Novel dopaminergic neurotransmission in the *Octopus* visual system

Amy Courtney[1], Ruth Styfhals[2], Marie Van Dijck[2], Jérôme Boulanger[1], Lieve Geenen[2], Maxence Lanoizelet[2], Iris Hardege[3], Mark Lassnig[2], Anna M. Jansson[1], Joseph Gehler-Rahman[1], Eduardo Almansa[4], Horst A. Obenhaus[5], Eve Seuntjens[2]*, William R. Schafer[1,2]*.

1. MRC Laboratory of Molecular Biology, Cambridge, UK.
2. Department of Biology, KU Leuven, Leuven, Belgium.
3. Department of Zoology, University of Cambridge, UK.
4. Oceanographic Centre of Canary Islands, Spanish Institute of Oceanography, CSIC, Tenerife, Spain.
5. Kavli Institute for Systems Neuroscience and Centre for Neural Computation, Norwegian University of Science and Technology, Trondheim, Norway.

* Corresponding Author

Summary

Octopus vulgaris, the common octopus, has a complex brain that evolved independently from that of vertebrates, raising the possibility that it may be built using novel circuit motifs or non-canonical neurochemistry. Through systematic characterization of octopus ligand-gated ion channel genes, we identified novel ionotropic receptors for two neurotransmitters, dopamine and acetylcholine, that play key roles in visual circuits. One of these, DopC1, encodes a dopamine-gated cation channel expressed in deeper layers of the optic lobe (inner granular layer and medulla). A second, AChRB1, encodes an acetylcholine-gated anion channel expressed in photoreceptors and dopaminergic outer granular layer neurons. Dopamine drives excitation, particularly in deeper, DopC1 enriched layers, and thereby may play an important role in feed-forward excitation, whereas acetylcholine evokes inhibition, possibly mediating negative feedback from deeper layers. The octopus visual system thus shows fundamental differences in both neurochemistry and wiring compared to mammals, implying distinct mechanisms of visual information processing.

32 # Introduction

33 Coleoid cephalopods, such as squid, cuttlefish and octopus, are notable for their large brains
34 and complex behaviour. For example, the nervous system of the common octopus, *Octopus*
35 *vulgaris*, contains approximately 500 million neurons[1], more than some mammals[2], and
36 supports intricate behaviours such as camouflage, tool use, visually-guided hunting, and
37 sophisticated learning and memory[3]. However, octopuses and humans diverged evolutionarily
38 approximately 600 million years ago, early in the bilaterian lineage, from a common ancestor
39 with a much simpler nervous system[4]. Thus, the complex brains of cephalopods appear to
40 have evolved independently from those of vertebrates. Gaining a better understanding of
41 cephalopod neural circuits will therefore shed light on the general principles that underpin
42 complex behaviour across species, as well as discover new biology and species-specific
43 innovations.

44 The visual system represents a particularly relevant opportunity to compare cephalopod and
45 vertebrate neural circuitry. Vision is an important sensory modality for cephalopods, driving
46 complex visually guided behaviours including camouflage, hunting, mating and learning[5].
47 Like vertebrates, cephalopods have two camera-type eyes that project visual scenes onto a
48 retina consisting of a single layer of photoreceptors, which direct their output to the cortex of
49 the optic lobe (OL), comprised of a superficial outer (OGL) and deeper inner (IGL) granular
50 layer. These neuronal cell layers are separated by a plexiform, neuropil layer that also
51 includes the end terminals of photoreceptors[6]. The OGL consists exclusively of neurons with
52 amacrine morphology, some of which receive inputs from photoreceptors and extend
53 processes laterally within the plexiform layer. The IGL contains a diverse population of
54 neurons, including amacrine-like cells that arborize in the plexiform layer, centrifugal cells
55 that send projections through the optic nerves back to the retina, and a variety of centripetal
56 cell types that extend processes through the plexiform layer and into the medulla[5].

57 The cortical layers of the OL, like the bipolar and granular cell layers in the mammalian
58 retina, are thought to carry out the first stages of visual information processing[7], and are
59 hence often referred to as the "deep retina". By way of comparison, in the vertebrate retina,
60 glutamatergic photoreceptors make excitatory retinotopic connections with off-bipolar cells
61 and inhibitory connections with on-bipolar cells; these bipolar cells in turn make excitatory
62 glutamatergic connections with retinal ganglion cells. Laterally-connected horizontal cells (in
63 the outer plexiform layer) and amacrine cells (in the inner plexiform layer) receive excitatory
64 glutamatergic inputs from photoreceptors or bipolar cells, and send inhibitory GABA or
65 glycinergic outputs to laterally-displaced cells in the layer[8]. The vertebrate retina is thus
66 characterized by both excitatory and inhibitory descending signaling, inhibitory lateral
67 signaling, and a lack of ascending feedback. It is unclear whether these microcircuit
68 properties are paralleled in the optic lobes of cephalopods.

69 To understand how cephalopod optic lobe circuits process information, it is necessary to
70 define the functional properties of their constituent neurons. In octopus, the main
71 neurotransmitters in the optic lobe are glutamate, acetylcholine (ACh) and dopamine[9,10].
72 While radiochemical experiments previously indicated that acetylcholine and dopamine are
73 synthesized in the retina (eye)[11], more recent electrophysiological recordings on optic lobe
74 slices from *Octopus vulgaris* indicate that photoreceptors release glutamate as an excitatory
75 neurotransmitter from terminals in the plexiform layer, and that this release is inhibited by
76 acetylcholine[12]. However, although inhibitory neuromodulatory effects of dopamine have
77 been reported in cuttlefish[13], the role of dopamine in octopus remains unknown. Likewise,
78 while glutamate responses in octopus are likely mediated by AMPA-like receptors[12], the
79 receptors mediating cholinergic and dopaminergic signaling in the octopus optic lobe have
80 not been identified. Since invertebrate nervous systems can express ionotropic receptors
81 whose ligands and ion selectivity differ markedly from the channels found in vertebrates[14-17],

82 the octopus brain might in principle use novel ion channels and unexpected neurochemistry
83 for fast neurotransmission.

84 In this study, we present the first steps toward mapping the pathways of chemical
85 neurotransmission in the *Octopus vulgaris* hatchling. By expressing octopus ion channel
86 genes in *Xenopus* oocytes, we characterised two new ionotropic receptors from the *Octopus*
87 visual system, including the first example of a dopamine-gated cation channel as well as an
88 anionic ACh receptor specifically expressed in dopaminergic neurons. Through functional
89 imaging from paralarval brain slices, we find that dopamine acts as a major excitatory
90 neurotransmitter in the optic lobe, mediating feed-forward signaling from the OGL to deeper
91 layers, while ACh acts as an inhibitory neurotransmitter that could enable ascending feedback
92 inhibition from the IGL to the OGL and eye. This work reveals fundamental differences
93 between the visual systems of octopus and vertebrates, at both the neurochemical and
94 microcircuit levels.

95 Results

96 Neurotransmitter usage in the eye and optic lobe

97 To investigate neuronal signaling in *Octopus vulgaris*, we focused on the newly-hatched
98 paralarva, or hatchling, as a tractable model. A single *O. vulgaris* spawning gives rise to
99 >100,000 progeny, which are around 2 mm long at hatching. While the hatchling brain is
100 smaller than that of the adult, with only ~200,000 neurons, it has the same lobular structure,
101 including a prominent optic lobe with a laminar cortex[18,19]. Moreover, transcriptomic studies
102 indicate that the paralarval brain shares most neural classes found in older animals [9,10,20].
103 Paralarvae rely heavily on vision for their survival, and they exhibit robust visually guided
104 behaviours including phototaxis, escape, colour change and prey capture[21].

105 We first quantified the spatial (co-)expression of all neurotransmitters in the eye and optic
106 lobe in detail. Based on previous data on neurotransmitter expression in the OL[9], we used
107 RNA fluorescence *in situ* hybridisation chain reaction (HCR) to probe the expression of six
108 neurotransmitter marker genes in the photoreceptors and the three layers of the OL. We used
109 the vesicular ACh transporter (vacht) as a marker for ACh, tyramine beta hydroxylase (tbh)
110 for octopamine, the vesicular GABA transporter (vgat) for GABA, tryptophan hydroxylase
111 (tph2) for serotonin, tyrosine hydroxylase (th) for dopamine, and the vesicular glutamate
112 transporter (vglut) for glutamate, and quantified (co-)expression in the optic lobe.

113 We observed highly specific patterns of expression for each neurotransmitter in the paralarval
114 visual system. In the eye, we observed positive signal only for glutamate (Fig. 1 a-f),
115 indicating that the photoreceptors are glutamatergic, consistent with earlier results showing
116 expression of glutamate receptors in the plexiform layer[12]. In the OL, we confirmed robust
117 expression of four neurotransmitters, categorising them into five cell types: cholinergic
118 (Chol: vacht^{+}), octopaminergic (Octo: tbh^{+}), exclusively glutamatergic (Glut: vglut^{+}/th^{-}),
119 exclusively dopaminergic (Dop: th^{+}vglut^{-}), and dopaminergic/glutamatergic co-expressing
120 (Dop/Glut: th^{+}vglut^{+}). Chol cells were absent from the OGL but represented a moderate
121 number of cells in the IGL (20%) and the highest proportion of cells in the medulla (59%)
122 (Fig. 1 g and i, Supplemental Fig. 1 a-c). Octo cells were relatively uncommon and were
123 found only in the OGL (10%) and IGL (4%) (Fig. 1 h and i, Supplemental Fig. 1 d-f). Glut
124 cells were found in all layers, representing 7% of cells in the OGL, 32% of cells in the IGL
125 and 55% in the medulla (Fig. 1 j and m, Supplemental Fig. 2 a-c). Dop cells were the main
126 cell type in the OGL (64%) and were also detected infrequently in the IGL (6%) and medulla
127 (2%) (Fig. 1 k, m, Supplemental Fig. 2 d-f). Dop/Glut cells, which expressed both dopamine
128 and glutamate, a cell type observed in transcriptomic studies from both hatchling and adult
129 brains[9,10], were the main cell type in the IGL (47%) and were less frequently seen in the OGL

130 (11%) and medulla (4%) (Fig. 1 l and m, Supplemental Fig. 2 g-i). GABA and serotonin
131 markers were detected only in a small number of medulla neurons, whose numbers we did
132 not quantify (Supplemental Fig. 2 j, k). In summary, the OGL was composed primarily of
133 Dop neurons along with other minor cell types, the IGL was a mixture of Glut, Chol and
134 Dop/Glut cells, and the medulla was mainly a mixture of Chol and Glut cells, consistent with
135 previous studies in *O. vulgaris* and *O. bimaculoides*[9,10].

136 A dopamine-gated cation channel expressed in the optic lobe

137 We next sought to functionally characterise neurotransmitter receptors expressed in the optic
138 lobe. We focused on cys-loop ligand gated ion channels (LGCs), a diverse family of
139 ionotropic receptors that includes the GABA-A, glycine, 5-HT3, and the nicotinic ACh
140 receptors of vertebrates as well as receptors with novel ligand specificity and ion selectivity
141 found in some invertebrate species[14-17]. We identified putative *Octopus* cys-loop LGCs using
142 comparative phylogenetics (Fig. 2 a) and used published single-cell RNA sequencing
143 (scRNA-seq) data [9] to focus on those expressed in the optic lobe. We expressed 41 of these
144 candidate *O. vulgaris* 'cys-loop' LGCs in *Xenopus* oocytes and used two-electrode voltage
145 clamp (TEVC) recordings to measure currents evoked by application of 18 candidate ligands.
146 Using this approach, we identified and characterised several candidate receptors activated by
147 neurotransmitters expressed in the optic lobe (Supplemental file 1).

148 Among these putative receptors was a homomeric channel encoded by the LOC115218923
149 gene, which was activated by dopamine and other monoamines (Fig. 2 b and Supplemental
150 Fig. 3 a). Expression analysis using scRNA-seq revealed that the LOC115218923 gene is
151 expressed across the brain, in particular within cell-types of the optic lobe (Supplemental Fig.
152 3 b, d). In TEVC recordings of LOC115218923-expressing oocytes, we observed currents in
153 response to dopamine (EC_{50}: 7.6 μM), norepinephrine (55 μM), epinephrine (35 μM),

154 serotonin (73 μM), tyramine (180 μM), and octopamine (18 mM)) (Fig. 2 c). This EC_{50} is
155 consistent with a synaptic receptor, as extrasynaptic receptors localized further from the
156 release sites often show an EC_{50} in the nM range. LOC115218923-expressing oocytes
157 showed the highest mean peak current when exposed to dopamine, with norepinephrine and
158 epinephrine (whose presence in the optic lobe has not been established) also showing large
159 currents and serotonin, tyramine and octopamine giving negligible responses (Fig. 2 d).
160 Interestingly, a metabotropic dopamine receptor agonist, apomorphine [22], acted not as an
161 agonist, but as an antagonist of dopamine-evoked responses (IC_{50}: 7 μM, Supplemental Fig. 4
162 a and c). When we performed ion substitution experiments, comparing the shift in reversal
163 potential (ΔErev) for a sodium-free or low-chloride solution compared to the standard buffer
164 (ND96), we observed a large reversal potential shift in the sodium-free solution and little
165 reversal shift in the low chloride-solution (Fig. 2 e). Thus, LOC115218923 appears to form a
166 dopamine-activated cation channel, which we designated DopC1 (for ***dop**amine-gated **c**ation*
167 channel).

168 Comparative phylogenetic analysis from diverse metazoan species indicated that DopC1 has
169 homologues throughout bilateria. In vertebrates its closest homologues are the α9/α10
170 nicotinic receptors, cation channels that are activated by ACh but not dopamine (Fig. 2 a).
171 DopC1 was not activated by ACh; moreover, nicotine, a potent antagonist for mammalian
172 α9/α10 receptors and agonist for other nicotinic channels, had no effect on DopC1-expressing
173 oocytes as either an agonist or antagonist (Supplemental Fig. 4 b and c). We also found direct
174 orthologs to DopC1 in many invertebrate species, including other cephalopods (*Euprymna*
175 *berryi*, *Sepia officinalis*), molluscs (*Pomacea canaliculata, Aplysia californica,* and *Lottia*
176 *gigantea*), an annelid (*Platynereis dumerilii*), a nematode (*Caenorhabditis elegans*), and
177 some arthropods (*Apis mellifera* and *Daphnia magna,* but not *Drosophila melanogaster*).
178 (Fig. 2 f). Expression of the DopC orthologs from *Aplysia* (LOC101853763), *Apis*

179 (LOC408525) and *Daphnia* (LOC116927457 and LOC116923538) in *Xenopus* oocytes also
180 produced homomeric channels activated by monoamines and not ACh (Fig. 3 a-d,
181 Supplemental Fig. 5 a-d). For all these channels, we found that dopamine had the lowest
182 EC_{50}, though in some cases other monoamines such as norepinephrine, serotonin and
183 tyramine also showed an EC_{50} in the μM range suggesting they might act as secondary
184 ligands (Fig. 3 e-h). Peak current analysis on oocytes expressing these invertebrate DopC1
185 orthologs likewise indicated that dopamine, norepinephrine and epinephrine evoked the
186 largest peak currents (Fig. 3 j). We also found a second DopC1-related sequence in *O.*
187 *vulgaris*, but this gene (LOC115215511/DopC2), while expressed in the optic lobe
188 (Supplemental Fig. 3 c and d), did not form a functional homomeric channel when expressed
189 in *Xenopus* oocytes (Supplemental Fig. 5 e). Taken together, these results suggest that in
190 addition to its well-established neuromodulatory action through metabotropic receptors,
191 dopamine may act as a fast excitatory neurotransmitter through ionotropic receptors in
192 octopus.

193 Dopaminergic excitation in the optic lobe

194 To explore the possible role of dopamine as a fast excitatory transmitter in the visual system,
195 we examined the spatial expression pattern of DopC1 in the hatchling brain of *O. vulgaris,*
196 with the goal of identifying cells whose activity might be stimulated by dopaminergic
197 neurotransmission. We performed quantitative HCR using probes for DopC1, either alone
198 (Fig. 4 a and b) or co-labelled with marker genes for the major optic lobe neurotransmitters
199 (Fig. 4 e-h, Supplemental Fig. 6 a-e). In these experiments we detected no expression of
200 DopC1 in the eye (Fig. 4 a), but observed widespread expression in the optic lobe (Fig. 4 a
201 and b), principally in the IGL and medulla. Specifically, DopC1 was expressed in 21% of
202 OGL neurons, 72% of IGL neurons, and 53% of medullar neurons (Fig. 4 b-d). In the OGL,
203 DopC1 expression was disproportionately observed in the minor cell types (Glut, Octo, or

204 Dop/Glut) and was rare in the predominant Dop cell type (Fig. 4 i, Supplemental Fig. 6 f).
205 DopC1 showed the highest expression in the IGL, where it was expressed in a majority of
206 each of the three major cell types in the IGL: 60% of Glut cells, 71% of Chol cells, and 92%
207 of Dop/Glut cells, the most common class in this layer (Fig. 4 i, Supplemental Fig. 6 g).
208 DopC1 was also detected in a majority of cells of the major medullar cell types, namely Chol
209 (64% DopC1 expressing) and Glut (55% DopC1 expressing). Other cell types with and
210 without DopC1 represented a very low percent of cells in the medulla (1-4%; Fig. 4 i,
211 Supplemental Fig. 6 h). DopC1 was also expressed throughout the central brain but at lower
212 levels compared to the optic lobe (Supplemental Fig. 7). In summary, DopC1 showed
213 relatively low expression in the OGL, but widespread expression in the IGL and medulla.

214 Based on this expression pattern, we hypothesised that dopamine might act as an excitatory
215 transmitter to stimulate activity in deeper layers of the OL. To test this hypothesis, we
216 performed calcium imaging on acute brain slices from 1-day *O. vulgaris* paralarvae,
217 measuring individual cell responses to exogenous dopamine (Supplemental Fig. 8 a). We
218 stimulated brain slices with 100 μM dopamine, followed by a high potassium solution
219 (HighK^+) as a control to identify actively-excitable cells, and characterized responses of
220 individual cells to dopamine. These experiments indicated that dopamine has a predominantly
221 excitatory role in the optic lobe (Fig. 5 a, b); excitatory responses to dopamine were seen in
222 all layers of the optic lobe, while inhibitory dopaminergic responses were rare in all layers
223 (≤1%). Notably, the proportion of cells showing excitatory dopaminergic responses, and the
224 kinetics of these responses, varied across the different optic lobe layers. For example, a
225 majority of cells in the IGL and the medulla showed positive responses to dopamine (83%
226 and 68% respectively), while many fewer cells in the OGL (44%) showed dopaminergic
227 excitation. Thus, excitatory dopamine responses were most common in the layers of the optic
228 lobe with pervasive DopC1 expression, and rarest in the OGL where DopC1 was most sparse.

229 When we analysed the responses more closely, we also observed differences between the
230 layers in the kinetics of dopamine response, reflected in the slope, relative amplitude, and
231 duration. In particular, the IGL showed the highest dopamine response amplitudes (relative to
232 HighK^+ response) compared to the other layers. Likewise, the IGL, along with the medulla,
233 showed longer lasting responses on average compared to the OGL (Fig. 5 c, Supplemental
234 Fig. 8 b-e). Finally, the slope of dopaminergic responses also varied between cells, with all
235 layers containing cells with 'shallow' slopes, indicating slow-increasing responses, as well as
236 those with steeper slopes, indicating fast-increasing responses (Fig. 5 d and e). The cells of
237 the IGL showed statistically steeper dopamine response slopes compared to the OGL and
238 medulla (Games-Howell post-hoc test, $p<0.0001$), and a higher proportion of cells with
239 steeply-rising slopes (Fig. 5 f, Supplemental Fig. 8 f). Thus, the rapid responses most
240 consistent with direct ionotropic activation by dopamine were most prevalent in the IGL, the
241 layer where DopC1 expression is most prevalent (Fig. 4 d). These results are consistent with
242 dopamine acting through DopC1 as a fast excitatory neurotransmitter in the IGL, and perhaps
243 also in the medulla.

244 An acetylcholine-gated anion channel expressed in dopaminergic neurons

245 To gain insight into how dopaminergic neurotransmission in the optic lobe is regulated, we
246 next focused on an LGC with specific expression in dopaminergic neurons. Analysis of
247 scRNA-seq data[9] revealed that a gene related to nicotinic ACh receptors, LOC115214201,
248 showed high and specific expression in dopaminergic clusters (Supplemental Fig. 9 a and b).
249 To investigate the functional properties of this channel, we expressed it in *Xenopus* oocytes
250 and performed TEVC recordings (Fig. 6 a, and Supplemental Fig. 10 c). We observed that
251 oocytes expressing the LOC115214201 gene, hereafter referred to as AChRB1, showed
252 currents in response to both ACh and choline, though the EC_{50} of 1.9μM for ACh was much
253 lower than that for choline (98 μM) (Fig. 6 b). This indicates that ACh likely acts as the

254 primary endogenous ligand, and the micromolar EC_{50} for ACh is consistent with AChRB1
255 acting as a synaptic receptor. To determine the ion selectivity of AChRB1, we performed ion
256 substitution experiments, as described previously for DopC1. For these experiments we used
257 the AChRB1 ortholog from *Octopus bimaculoides,* as it expressed more robustly in oocytes
258 compared to the *O. vulgaris* gene while sharing the same ligand specificity properties
259 (Supplemental Fig. 10 d and e). We found that the AChRB1 channel showed a large and
260 significant shift in reversal potential in the low-chloride solution; in contrast, replacement of
261 the normal buffer with a sodium-free solution caused no significant shift (Fig. 6 c). Thus,
262 octopus AChRB1 appears to function as an anionic channel capable of mediating inhibitory
263 cholinergic neurotransmission.

264 Our comparative phylogenetic analysis of cys-loop LGCs from metazoans placed this gene
265 within a group of anionic ACh-gated channels previously functionally characterised in the
266 mollusc *Lymnaea stagnalis*[23] (AChRB), and the platyhelminth *Schistosoma mansoni*[24] (Fig. 2
267 a). Our phylogenetic analysis also found direct orthologs in other molluscs (*Aplysia*
268 *californica, Pomacea canaliculata, Lottia gigantea*), platyhelminths (*Schmidtea*
269 *mediterranea*) and annelids (*Platynereis dumerilii, Capitella teleta*). Despite being related to
270 cationic nicotinic ACh-gated channels, all genes within this group contain a PAK (proline-
271 alanine-lysine) motif in the pore lining region similar to that found in anion-permeable
272 GABA-A and glycine receptors (Supplemental Fig. 9 c) that has been linked to chloride
273 selectivity[25]. Thus, the AChRB family may form ACh-gated anion channels in many
274 Lophotrochozoan phyla. Our phylogenetic analysis identified two other members of this
275 family (LOC115229990/AChRB2 and LOC115212977/ AChRB3) in *O. vulgaris*, however,
276 these did not show currents when expressed as homomeric channels in oocytes (Supplemental
277 Fig. 10 a and b).

278 **Acetylcholine acts as an inhibitory transmitter in the optic lobe**

279 To explore the effect of AChRB1 on octopus visual circuits, we first investigated its
280 expression pattern in the brain of *O. vulgaris* paralarva through quantitative HCR. We
281 observed widespread expression of the AChRB1 gene in the eye (85% of photoreceptor
282 cells), in the OGL and IGL (56% and 51% respectively), and in a low proportion of medulla
283 cells (4%) (Fig. 6 d-f). To investigate the expression pattern of AChRB1 in the optic lobe in
284 more detail, we performed multiplex HCR of AChRB1 in combination with marker genes for
285 visual system neurotransmitters (Fig. 6 g-j, Supplemental Fig. 11 a-e). Within the OGL,
286 AChRB1 was expressed in most of the Dop neurons (70%), the most common cell type in the
287 layer. It was also expressed a majority of the Octo cells (76%), as well as in around half of all
288 Dop/Glut OGL cells (49%; Fig. 6 k, Supplemental Fig. 11 f). In the IGL, AChRB1 was
289 expressed in most Dop/Glut cells (67%) the most common cell type in the layer, in a smaller
290 fraction of Chol (30%) and Glut cells (44%), and not at all in Octo cells (Fig. 6 k,
291 Supplemental Fig. 11 g). AChRB1 was expressed in very few medulla cells (7% of Glut
292 cells) and some central brain cells (Fig. 6 k, Supplemental Fig. 11 h, Supplemental Fig. 12).
293 To summarise, we observed AChRB1 expression most prominently in three cell types: Glut
294 photoreceptors in the eye, Dop amacrine cells in the OGL, and Dop/Glut cells in the IGL.

295 Since all three of these cell types are potential recipients of synaptic input from cholinergic
296 neurons in the IGL and/or the medulla[26], and since scRNA-seq data indicated that cationic
297 nicotinic ACh-gated channels are not highly expressed in dopaminergic clusters
298 (Supplemental Fig. 13 a), we hypothesised that ACh might act through AChRB1 as an
299 inhibitory neurotransmitter in the octopus visual system. To test this hypothesis, we
300 performed calcium imaging on acute brain slices from *O. vulgaris* paralarvae following acute
301 application of ACh, using the same protocol used for dopamine. We indeed observed mostly
302 inhibitory effects of ACh on optic lobe calcium activity (Fig. 7 a-e, Supplemental Fig. 14).

303 ACh-mediated inhibition was observed in all layers of the OL: 10% of OGL cells, 5% of IGL
304 cells, and 19% of medulla cells (Fig. 7 f); in contrast, excitatory responses to ACh were
305 observed in less than 2.6% of all cells in each layer while other recorded cells had no
306 detectable response (Fig. 7 f). The proportion of cells experiencing inhibition by ACh is
307 likely underestimated in our experiments due to the absence of baseline activity which largely
308 masks inhibition in our calcium imaging preparation. However, the fact that ACh elicited
309 primarily inhibitory, rather than excitatory, responses in the optic lobe is consistent with
310 AChRB1 mediating inhibitory neurotransmission in visual circuits.

311 **Discussion**

312 In this study, we have begun to map the microcircuit architecture and function of the visual
313 system of the *Octopus vulgaris* paralarva, with the goal of linking neurotransmitters, their
314 receptors, and their physiological effects. In particular, we have defined the physiological
315 properties of receptors for key optic lobe neurotransmitters, dopamine and ACh, and localised
316 receptor expression relative to their neurotransmitter ligands within the eye and optic lobe.
317 Through imaging of dopamine and ACh responses in different layers of the optic lobe, this
318 work has provided new insights into the molecular and circuit mechanisms underlying visual
319 processing in octopus.

320 These experiments revealed that dopamine, unexpectedly, functions as a major excitatory
321 neurotransmitter in the optic lobe. Calcium imaging of octopus brain slices following
322 application of dopamine showed acute activation in all optic lobe layers, most prominently in
323 the IGL. This activation correlates with the expression of DopC1, a newly-characterised
324 dopamine-gated cation channel found in nearly all IGL neurons, as well as some OGL
325 neurons and about half of medullar neurons. Not only do the vast majority of IGL neurons
326 (>80%) show increased activity in response to dopamine, the neurons in the IGL also showed

327 consistently faster-increasing responses, suggesting direct activation via ionotropic DopC1
328 receptors. Most neurons in the OGL are dopaminergic, with axons juxtaposed with the
329 dendrites of DopC1-expressing IGL neurons in the plexiform layer. This strongly suggests
330 that signaling between neurons in the OGL and higher-order neurons in the IGL involves
331 dopaminergic excitatory transmission, mediated by DopC1.

332 The DopC receptor identified in this study defines a new class of monoamine-gated cation
333 channel whose members likely play important roles in excitatory neurotransmission in
334 invertebrates. Excitatory currents activated by dopamine have been described previously in a
335 gastropod mollusc, *Helisoma trivolvis*[27], but the molecular identity of the receptors mediating
336 these currents was not known. Since the DopC1 homologue from *Aplysia* is also monoamine-
337 activated, we hypothesise that a DopC-related channel might also be responsible for
338 dopaminergic excitatory transmission in gastropods. Although dopamine-gated channels have
339 been previously identified in *C. elegans*, these are anionic channels that belong to a GABAA-
340 related LGC subfamily that is specific to nematodes[15,16,28]. In contrast, cationic DopC1
341 receptors are homologous to vertebrate α9/10 nicotinic receptors and appear to form
342 monoamine-gated channels in phyla ranging from lophotrochozoans such as molluscs and
343 annelids to ecdysozoans such as arthropods and nematodes. Our results therefore suggest that
344 in octopus, as well in many other invertebrates, dopamine not only acts as a slow
345 neuromodulator through G-protein coupled receptors, but also as a fast excitatory
346 neurotransmitter through DopC-related channels.

347 Our observation that dopamine is largely excitatory in the *O. vulgaris* optic lobe was
348 surprising given a previous report[13] that cuttlefish optic lobe neurons showed a decrease in
349 spontaneous activity in a small sample of optic lobe neurons following dopamine application.
350 While the authors make no claims about directly evoked dopaminergic currents, we were
351 unable to confirm or refute these observations in our calcium imaging preparation due to its

352 inability to resolve spontaneous (subthreshold) events. Alternatively, since octopods and
353 decapods are separated by 250 million years of evolution, it is possible that dopamine may
354 play different roles in the cuttlefish and octopus optic lobes. Both *Euprymna berryi* (squid)
355 and *Sepia officinalis* (cuttlefish) have DopC1 homologs[29,30]; thus, it will be interesting to
356 investigate how dopamine signaling functions in the visual circuits of these more distantly-
357 related cephalopod species.

358 In the context of the optic lobe circuitry, dopaminergic transmission through DopC1 appears
359 to play a key role in descending excitatory pathways that propagate visual information from
360 first-order to higher-order neurons. Previous work has shown that cephalopod photoreceptors
361 (in contrast to those of vertebrates) are excited by light[7,31], have large presynaptic output
362 terminals in the superficial plexiform layer of the optic lobe that contact the dendrites of OGL
363 neurons[26]. While these photoreceptors were previously thought to be cholinergic[11,31], recent
364 scRNA-seq data from squid[29] along with our HCR results from *Octopus vulgaris* indicate
365 that they release the excitatory neurotransmitter glutamate. Since most OGL neurons are
366 dopaminergic, we infer that these neurons relay and/or filter depolarizing signals from the
367 photoreceptors to the dendrites of DopC1-expressing IGL neurons found deeper in the
368 plexiform layer. Dopaminergic transmission may thus facilitate the retinotopic ON pathways
369 recently described in *O. bimaculoides* during light stimulation[7]. Since some IGL neurons may
370 also receive direct, glutamatergic excitatory input from the photoreceptors as well as feed-
371 forward, dopaminergic excitation from OGL neurons, dopaminergic signaling may serve to
372 amplify the signal between the OGL and IGL, as was observed in *O. bimaculoides* calcium
373 imaging experiments[7].

374 Dopaminergic signaling may also be important to propagate excitatory signaling between the
375 IGL and the medulla. In particular, the DopC1-expressing Dop/Glut IGL neurons produce
376 two excitatory neurotransmitters, glutamate[12] as well as dopamine. Many neurons in the

377 medulla express DopC1, and many also undergo activation by dopamine, in some cases with
378 rapid kinetics (Fig. 5 f). Since very few neurons in the medulla synthesize dopamine, the
379 dopaminergic inputs to the medulla are therefore likely to come primarily from Dop/Glut
380 neurons in the IGL. Thus, the Dop/Glut neurons may correspond to the centripetal neurons
381 described by Young, serving as descending excitatory relays of visual information from
382 second-order neurons of IGL to third-order neurons of the medulla (Fig. 7 g).

383 Our results also define a role for ACh as an inhibitory neurotransmitter in the octopus optic
384 lobe. Although inhibition is intrinsically difficult to detect using calcium imaging, we
385 observed clear evidence of cholinergic inhibition in all layers of the optic lobe; in contrast,
386 we observed little evidence for cholinergic excitation. This cholinergic inhibition correlates,
387 particularly in the OGL and IGL, with the expression of an ACh-gated anion channel,
388 AChRB1. AChRB1 is a nicotinic receptor whose pore domain is selective for anions rather
389 than cations and is homologous to previously described ACh-gated anion channels in the
390 gastropod *Lymnaea* and the platyhelminth *Schistosoma*[23,24]. The expression of AChRB1 in
391 the photoreceptors and neurons of the optic lobe cortex correlates with previous reports that
392 ACh caused inhibition in the plexiform layer of *O. vulgaris* adult optic lobe slices, while
393 nicotinic receptor agonists such as α-bungarotoxin and atropine had no effect[32]. We note that
394 we also identified classical nicotinic cationic ACh-gated channels in *O. vulgaris*, though they
395 are not highly expressed in the optic lobe. Interestingly, ACh-gated anion channels have also
396 been found in nematodes, but these are unrelated to AChRB1 and more closely related to
397 GABA-A-like receptors[17]; indeed, AChRB-like channels, unlike DopC-like channels, have
398 been found only in lophotrochozoan nervous systems.

399 In contrast to dopamine and glutamate, which appear to function primarily in descending,
400 feed-forward pathways in the optic lobe, acetylcholine appears to act in ascending, feedback
401 pathways. For example, we observed widespread expression of AChRB1 in the OGL,

402 particularly in Dop and Dop/Glut cells; thus, ACh likely inhibits neurons releasing the two
403 major excitatory neurotransmitters in the OGL, dopamine and glutamate. Neither the OGL
404 nor the retina contains cholinergic neurons; thus, the cholinergic input neurons that act on
405 AChRB1-expressing neurons in the OGL must be IGL or medullar neurons that project
406 processes into the plexiform layer. In addition, we observed AChRB1 expression in
407 photoreceptors, and previous reports indicate that ACh indeed exerts inhibitory effects on
408 photoreceptor terminals in the plexiform layer. Thus, cholinergic neurons from the IGL
409 appear to inhibit both photoreceptor terminals and dopaminergic OGL neurons in the
410 plexiform layer. In addition, if cholinergic neurons correspond to the centrifugal cells
411 reported by Young [26], they might also inhibit photoreceptors in the retina itself, or provide
412 lateral inhibition to neighbouring IGL cells that express AChRB1(Fig. 7 h).

413 Since cholinergic inhibition was also seen in the medulla, it is possible that acetylcholine may
414 function in descending inhibitory pathways as well. In *Octopus bimaculoides*, it has been
415 shown that OFF retinotopic pathways first appear in the medulla[7]; thus cholinergic inhibition
416 might carry out the required sign inversion between the IGL and medullar layers. It should be
417 noted however that AChRB1 itself does not show detectable expression in the medulla; thus,
418 the cholinergic inhibition in medullar neurons may be mediated by a different, yet-
419 unidentified inhibitory ACh receptor. Alternatively, AChRB1 might act indirectly to inhibit
420 medullar neurons by inhibiting the output terminals of excitatory centripetal neurons
421 projecting from the IGL, similar to its inferred role at photoreceptor terminals in the
422 plexiform layer.

423 The octopus visual system, like those of other cephalopods, shares important common
424 features with that of vertebrates; indeed, the camera-like eye and laminar optic lobe cortex
425 (OGL and IGL, sometimes called the "deep retina") are often cited as examples of convergent

426 evolution. However, at the microcircuit level our work suggests important differences may
427 exist between the wiring of the octopus and mammalian visual pathways. In particular, the
428 expression of inhibitory AChRB channels in photoreceptors and lower-order dopaminergic
429 neurons implies the existence of ascending, negative feedback pathways in the first steps of
430 octopus visual processing, from the inner granular layer and/or medulla to the OGL and the
431 eye. This is in marked contrast to the mammalian retina, where no ascending pathways are
432 found in the first three layers of the visual circuitry. Our results also imply an inverted
433 polarity for lateral signaling in at least some neurons involved in early visual processing. In
434 particular, dopaminergic OGL amacrine cells direct excitatory outputs (to DopC1-expressing
435 targets) and receive inhibitory inputs (from cholinergic neurons via AChRB1) in the
436 plexiform layer. In contrast, laterally-projecting horizontal and amacrine cells of the
437 vertebrate retina receive excitatory glutamatergic inputs and make inhibitory GABAergic
438 outputs in the inner and outer plexiform layers[8] (Fig. 7 i). Thus, the visual circuitry of
439 *Octopus* may contain novel circuit motifs, such as cholinergic-dopaminergic inhibitory
440 feedback loops and reverse-polarity amacrine cells, that differ from those found in the
441 mammalian retina.

442 Coleoid cephalopods have become of great interest to neuroscientists due to their independent
443 evolution of intelligence and innovative behaviours. In addition to their well-established
444 differences in systems-level organisation, our work here has provided functional and
445 evidence that cephalopod and vertebrate visual systems are also profoundly different at the
446 neurochemical and microcircuit levels. As a result of evolutionary diversification of the
447 ligand and ion selectivity of ionotropic receptors, the octopus uses dopamine as a fast
448 excitatory neurotransmitter, and ACh as an inhibitory transmitter, in the optic lobe. Likewise,
449 the circuitry that carries out the earliest stages of visual processing in octopus makes use of
450 microcircuit motifs that are not found in the vertebrate retina, suggesting they may use

innovative circuit mechanisms for processes such as object identification and motion detection. Going forward, it will be interesting to identify computational principles that are shared between the visual circuits of cephalopods and vertebrates, as well as those unique to the complex, "alien" brain of the octopus.

Methods

Data and Code availability

All custom code developed for this study has been deposited to GitHub (see below). The phylogenetic analysis data is available in supplemental file 2-4. The HCR probe sequences are available in supplemental file 5. All images used for quantitative HCR are shown in main and supplemental figures. All other data are available from the authors upon request.

Octopus vulgaris paralarvae

Adult male and female wild caught *O. vulgaris* were maintained and mated in the Oceanographic Center of the Canary Islands Instituto Español de Oceanografía (IEO-CSIC, Tenerife, Spain) according to Almansa et al.[33] and upon spawning embryos were shipped to Belgium. Embryos were then incubated until hatching in a closed system in the Laboratory of Developmental Neurobiology (KU Leuven), Belgium (ref). Animals used in this study were from spawnings that occurred between September 2021 and November 2024. All procedures involving adults and hatchlings were approved by the ethical board and competent authority on animal experimentation from CSIC (permit CEIBA 1377-2023 and 1610-2024) and KU Leuven (permit P080/2021), in compliance with Directive 2010/63/EU.

471 ## Octopus genomes

472 At the conception of this project a high-quality genome/transcriptome did not exist for
473 *Octopus vulgaris* and thus the genome/transcriptome of *Octopus sinensis* (*ASM634580v1*)
474 was used for designing primers for PCR and probes for HCR (more details below). *Octopus*
475 *sinensis* is the most closely related octopus species to *Octopus vulgaris* and it was reported
476 that there is only a 3.21% difference between the mitogenomes [34]. In addition, the *O. vulgaris*
477 scRNA-seq [9] was performed on *Octopus vulgaris* 1-dph paralarval brains but was mapped to
478 the *Octopus sinensis* genome. At later stages of the project a high-quality
479 genome/transcriptome was published for *Octopus vulgaris* (*PRJEB61268,* [34] and was
480 incorporated into the phylogenetic analysis.

481 ## Comparative phylogenetics of metazoan LGCs

482 **Identifying LGCs in Octopus and diverse metazoan phyla**

483 Cys-loop LGC protein sequences were identified using the PFAM domain PF02931, and the
484 following publicly available sequence datasets were selected to include species
485 representatives from all the major phyla. *Homo sapiens* (GRCh38.p14), *Danio rerio*
486 (GRCz11), and *Ciona intestinalis* (GCA_000224145.1), were included as Chordate
487 representatives. *Saccoglossus kowalewskii* (PRJNA42857) was the hemichordate
488 representative. *Strongylocentrotus purpuratus* (Spur_5.0) was the Echinoderm representative.
489 *Octopus sinensis (ASM634580v1)*, *Octopus bimaculoides (ASM119413v2)*, *Octopus vulgaris*
490 *(PRJEB61268)*, *Euprymna berryi* (PRJEB52690), *Sepia Officinalis* (PRJNA1091451),
491 *Aplysia californica (AplCal3.0)*, *Lottia gigantea (Lotgi1)* and *Pomacea canaliculate*
492 (ASM307304v1) represented the Mollusca. Three octopus genomes were used to ensure we
493 didn't miss any LGCs that were not annotated correctly. Two sequences from *Lymnaea*
494 *stagnalis* were also included as they were functional characterized as anionic and cationic

495 ACh-gated channels[23]. *Platynereis dumerilli (GCA_026936325.1)*, *Hellobdella robusta*
496 *(Helro1)*, and *Capitella teleta (GCA_000328365.1)* were included as annelid representatives.
497 Three sequences from *Alvinella pompejana* were also included as they had been previously
498 functionally identified as glycine and proton-gated channels[35]. *Schmidtea mediterranea*
499 (PRJNA379262) and *Schistosoma mansoni* (PRJEA36577) were included for Platyhelminths.
500 *Drosophila melanogaster (BDGP6.46)*, *Daphnia magna (ASM2063170v1.1)*, and *Apis*
501 *mellifera* (Amel_HAv3.1) were included for Arthropods. *Caenorhabditis elegans*
502 (PRJNA13758) and *Brugia malayi* (PRJNA10729) were included for nematodes.
503 *Nematostella vectensis (PRJEB51373)*, and *Clytia hemisphaerica* [36] represented the
504 Cnidarians. All sequences were downloaded from Biomart [37], except for *O. vulgaris* where
505 we ran interproscan (v5.33) ourselves and *C. hemisphaerica* where we downloaded the
506 sequences from MARIMBA (http://marimba.obs-vlfr.fr/home). Jaiteh et al. [38] determined that
507 Ctenophora, Proifera and Placozoa had no LGCs in their genomes. We also included all
508 metazoan sequences from the Jaiteh et al., 2016 dataset, which included 31 representative
509 metazoan species.

510 **Alignment and tree generation**

511 LGCs have four transmembrane domains, and thus partial sequences with less than three
512 transmembrane domains were removed. Transmembrane domains were predicted using
513 TMHMM [39]. The longest isoform for each gene was manually identified and others were
514 removed. Alignment was performed using MAFFT (v7.505) with E-INS-i parameters
515 allowing for large gaps [40], as Jaiteh et al., [38], determined this was an effective approach for
516 aligning LGC protein sequences. The alignment was trimmed using Trimal (v1.4.1) gappyout
517 method [41]. The alignment was manually assessed to ensure each sequence had the 'cys-loop
518 region', and the four transmembrane domains. Any sequences with large inserts were
519 removed iteratively until a satisfactory alignment was achieved.

520 Phylogenies were generated using IQ-TREE v2.1.4_beta with 1,000 ultra-fast bootstraps [42].
521 The tree model was calculated using IQ-TREE's ModelFinder implementation according to
522 Bayesian inference criterion (BIC) and Q.yeast+F+R10 was used.

523 **Tree visualization and annotation**

524 The tree was visualized using TreeViewer [43] and species illustrations were either generated
525 by authors or sourced from Phylopic (phylopic.org) (Fig. 2 a and e). LGCs contain a
526 characteristic 'cys-loop' region in their extracellular ligand binding domain which contains
527 13 residues flanked by two cysteines that create a disulphide bond. Jaiteh et al. previously
528 characterised a 'cys-less' group of LGCs which lack these cysteines in eukaryotes (many
529 protists and a few invertebrates) [38]. We used this cys-less group to root the tree. We assigned
530 a functional annotation for the primary ligand to any subfamily where one or more sequences
531 had been previously functionally characterized in a heterologous expression system. Our
532 LGC tree, and others in the literature, split between GABA-A-like anionic LGCs and
533 Nicotinic-ACh-like cationic LGCs. However, within these anionic/cationic subfamilies some
534 exception exists and thus the ion selectivity of these exceptional cases are also highlighted
535 where functional data exists. The references associated with the functional annotations of
536 each sequence can be found in supplemental file 2. Our LGC dataset contains 1197
537 sequences, the alignment is available as supplemental file 3 and the full tree is available as
538 supplemental file 4.

539 Two-electrode voltage clamp recordings of LGCs in *Xenopus* oocytes

540 ***Xenopus* laevis plasmids**

541 *O. vulgaris* RNA was extracted from 15 1-dph paralarvae using Tri-reagent (Invitrogen) and
542 the Qiagen Micro kit (Qiagen). *Daphnia magna* RNA was extracted from 20 adults using Tri-
543 reagent (Invitrogen) and the Qiagen Micro kit (Qiagen). cDNA for both *O. vulgaris* and *D.*

544 *magna* was synthesised using the Superscript III RT (Invitrogen) kit, and LGC sequences
545 were amplified using Q5 polymerase (NEB, MA, USA). The cDNA sequence for the DopC1
546 gene from *Aplysia californica* (LOC101853763) and *Apis mellifera* (LOC408525) were
547 synthesised using the GeneArt Gene Synthesis Service (Thermo Fisher Scientific, Waltham,
548 MA, USA). LGC cDNA sequences from *O. vulgaris, D. magna, A. californica and A.*
549 *mellifera* were then inserted into the KSM backbone using HiFi assembly (NEB, MA, USA).
550 The KSM backbone contains *Xenopus* β-globin UTR regions and a T3 promoter. The cDNA
551 sequence of the *Octopus bimaculoides* AChRB1 (LOC106879694/XM_052969792.1) gene
552 was synthesized as a geneblock DNA fragment by IDT-DNA Inc (Coralville, IA, USA) with
553 a Kozak transcriptional start signal (GCCACC) added immediately upstream of the initial
554 methionine codon. This fragment was inserted between the two Sma I restriction enzyme
555 sites of pGEMHE [44] by Gibson assembly.

556 ***Xenopus laevis* oocytes and RNA injection**

557 Defolliculated *Xenopus Laevis* oocytes were acquired from EcoCyte Bioscience and
558 maintained in ND96 solution (in mM: 96 NaCl, 1 MgCl2, 5 HEPES, 1.8 CaCl2, 2 KCl) at
559 16°C until RNA injection. KSM plasmids were linearized with NotI, and 5'-capped cRNA
560 was synthesized *in vitro* using the T3 mMessage mMachine transcription kit (Thermo Fisher
561 Scientific, CA, USA). The pGEMHE plasmid was linearised with Eco53kI and synthesized *in*
562 *vitro* using the T7 mMessage mMachine transcription kit (Thermo Fisher Scientific, CA,
563 USA). The RNA was subsequently purified with the GeneJET RNA purification kit (Thermo
564 Fisher Scientific, CA, USA). Defolliculated *Xenopus* oocytes were individually placed in v-
565 bottom 96-well plates and injected with RNA using the Roboinject system (Multi Channel
566 Systems GmbH, Reutlingen, Germany). Each oocyte was injected with 50 nl RNA solution at
567 a concentration of 250 ng/µl-500 ng/µl, depending on the construct. Following injection, the
568 oocytes were incubated in ND96 at 16°C for 2-4 days prior to recording.

569 **Two-electrode voltage clamp recording and analysis**

570 TEVC recordings were performed either using the automated Robocyte2 system (Multi
571 Channel Systems, Reutlingen, Germany) or a manual system (OC-725D amplifier).
572 Recording electrodes for the Robocyte2 system were purchased from Multichannel systems
573 and typically had a resistance of 0.7-2 MΩ. Recording electrodes for the manual system
574 (GC120TF-10, Warner Instruments) were pulled using a P-1000 Micropipette Puller (Sutter,
575 Ca, USA) with the same resistance as above. Recording electrodes were filled with 1.5M
576 KCl and 1 M acetic acid. Oocytes were clamped at -60 mV and continuous recordings were
577 done at 500 Hz. Recordings on the Robocyte2 system were collected using the Robocyte2
578 control software and the data was extracted using the Robocyte2+ analysis software.
579 Recording on the manual system were collected using WinWCP software. The following
580 ligands were applied to all receptors described in the paper at 1mM during initial experiments
581 to determine their primary/secondary ligands. All ligands were prepared in ND96 solution
582 and were applied for 7 seconds. Fresh ND96 solution then applied for 40s to wash out the
583 ligand before applying the next ligand. The ligands used for screening were acetylcholine
584 chloride (ACh, sc-202904, Santa Cruz Biotechnology,USA), L-Glutamic acid monosodium
585 salt monohydrate (Glut, 49621, Merck, Germany), γ-Aminobutyric acid (GABA, A2129,
586 Merck, Germany), Glycine hydrochloride (Gly, G2879, Merck, Germany), dopamine
587 hydrochloride (Dop, H8502, Merck, Germany), DL-norepinephrine hydrochloride (Norepi,
588 A7256, Merck, Germany), (+/-)-Epinephrine hydrochloride (Epi, E4642, Merck, Germany),
589 Tyramine hydrochloride (Tyra, T2879, , Merck, Germany), (+/-)-Octopamine hydrochloride
590 (Octo, O0250, Merck, Germany), serotonin hydrochloride (5-HT, sc-201146A, Santa Cruz
591 Biotechnology, USA), Choline chloride (Chol, C1879, Merck, Germany), Betaine
592 hydrochloride (Bet, B3501, Merck, Germany), adenosine (Ado, 01890, Merck, Germany),
593 Adenosine 5′-triphosphate disodium salt hydrate (ATP, A26209, Merck, Germany), β-alanine

594 (β-al, 146064, Merck, Germany), D-serine (D-ser, S4250, Merck, Germany), and L-Lysine
595 (Lys, L5501, Merck, Germany).

596 Dose response analysis was performed by first perfusing the oocytes with ND96 to estimate
597 resting potential of the oocytes. Then the ligand solution was applied for 7 seconds and then
598 ND96 solution was applied again for 40 seconds to bring the oocyte back to resting potential.
599 This was repeated for all doses of the ligand from low to high concentrations. The dose
600 response results combined data from 3-7 oocytes and the data was normalised to the largest
601 current in each oocyte. Normalized mean and standard deviation where then imported into
602 GraphPad prism where data was plotted and EC_{50} values were calculated by fitting to the Hill
603 equation using three parameter slopes to obtain the highest degree of fit.

604 Ion selectivity analysis was performed using ND96 solution, a sodium-free solution (96mM
605 NMDG, 2mM KCl, 1.8mM CaCl2, 5mM HEPES, 1mM MgCl2) and a low-chloride solution
606 (96mM Na Gluconate, 2mM KCl, 1.8mM CaCl2, 5mM HEPES, 1mM MgCl2). A voltage
607 ramp from -150 mV to +30 mV was applied to oocytes expressing the receptor of interest in
608 the presence of the following solutions in the following order; ND96, ND96+ligand, sodium-
609 free, sodium-free +ligand, low-chloride, low-chloride +ligand. The EC_{50} concentration of the
610 primary ligand was used in each case, either ACh for AChRBs and dopamine for DopCs.
611 Analysis was performed using a custom python script (https://github.com/hiris25/TEVC-
612 analysis-scripts).

613 Peak current analysis was performed by exposing individual oocytes expressing specific
614 LGCs with 1mM dopamine, serotonin, norepinephrine, octopamine, epinephrine, and
615 tyramine in this order and the current was normalized to the peak current in each oocyte.
616 After exposing each oocyte to these ligands, dopamine was applied again at 1mM to ensure
617 the channel had not desensitized. The mean and standard deviation per channel and per ligand
618 were then calculated and the data was plotted in Graphpad Prism.

619 ## Single cell RNA sequencing analysis

620 All scRNA-seq results were from the dataset detailed in Styfhals et al [9]. Data visualisation
621 was performed in Seurat v4 [45].

622 ## RNA fluorescent *in situ* hybridisation chain reaction (HCR)

623 1-dph paralarvae were sedated in 2% ETOH/artificial seawater, humanely killed in 4%
624 EtOH/artificial seawater and fixed overnight in 4% paraformaldehyde (PFA) in phosphate-
625 buffered saline treated with DEPC (PBS-DEPC). RNA fluorescent *in situ* hybridization chain
626 reaction (HCR) was performed as previously described [46]. In brief, parlarvae were embedded
627 in paraffin following progressive dehydration and sectioned with a paraffin microtome
628 (Thermo Scientific, Microm HM360) to obtain 6-µm-thick transversal sections. Prepared
629 tissue slides were then used to perform hybridization chain reaction experiments (HCRv3.0).
630 Probe sets were designed with the insitu_probe_generator [47], followed by automated blasting
631 and formatting to minimize off-target hybridization with a custom script [48] and synthesised
632 by IDT (DNA oPools™, Integrated DNA Technologies). Probes were blasted against the *O.*
633 *sinensis* (PRJNA551489) or the *O. vulgaris* transcriptome (PRJEB61268) [34] to ensure
634 specificity. Each probe was tested on multiple occasions on different batches of paralarvae
635 and the expression pattern reproducible. These probes were applied at 0.9 pmol per slide.
636 Upon completion of the HCR protocol, DAPI staining was performed (32670-5MG-F,
637 Merck), slides were mounted with a cover slip (Epredia, 24 x 55 m #1) using Mowiol and
638 allowed to dry for 24 h at 18°C before being stored at 4°C until imaging. All probes
639 sequences are included in supplemental file 5.

640 **HCR image acquisition**

641 Confocal microscopy was performed using a spinning disk system (Andor BC43, Oxford
642 Instruments) with 405 nm, 562 nm, 600 nm, and 700 nm excitation lasers (respectively blue,

643 green, red and far red). Images were acquired with a 60X/1.42 NA oil-immersion objective
644 (Nikon CFI Plan Apochromat Lambda D) and an sCMOS camera (Oxford Instruments, 6.5
645 µm pixel size, 82% QE) at a 0.3 µm z-step.

646 **HCR image analysis**

647 All HCR images were prepared for publication by cropping and adjusting brightness/contrast
648 using Imaris Software (Oxford Instruments) and Fiji [49]. HCR fluorescence was not visible in
649 the plexiform layer or other neuropil regions and localised around the nuclei, therefore a
650 custom python script was written to quantify HCR fluorescence within the nuclear regions of
651 cells in the *O. vulgaris* paralarval brain (https://github.com/jboulanger/fish-octopus). The
652 expression pattern was consistent across replicates and thus quantification was performed on
653 individual slices. The cell pose pre-trained 'Nuclei' model was used to segment nuclei (DAPI
654 channel) in 3D from the Z-stack projections[50]. Each 6µm section contained ~2 layers of
655 densely packed nuclei. The Napari polygon tool was used to manually define anatomical
656 regions (i.e. OGL, IGL, Med, CB) (https://github.com/napari/napari). A difference of
657 Gaussian filter with sigma [0.5,1,1 pixels] along the z,y,x axes was used to identify positive
658 fluorescent signals from background signal. The filtering was followed by a Relu activation
659 defined as $\max\left(0, \frac{x}{s} - 4\right)$ where the standard deviation s is estimated using a maximum
660 absolute deviation to define a score. The mean fluorescence of this score for each fluorescent
661 channel within the area of the 3D segmented nuclei was recorded. A second threshold was
662 then manually defined for each gene to determine positive/negative expression within a
663 segmented nucleus.

664 ## Calcium imaging of acute paralarval brain slices

665 **Reagents and solutions**

666 Octomedia was prepared by starting with 500 ml L-15, Leibowitz, with L-glutamine (Sigma,
667 MFCD00217482) and then adding the following components (in mM) NaCl: 214.04,
668 $MgSO_4x7H_2O$: 26.17, KCl: 4.61, NaHCO3: 2.29, $MgCl_2x6H_2O$: 28.04 , D-glucose: 38.08, and
669 $CaCl_2x2H_2O$: 10.12. Taking the composition of L-15 into account the final concentrations
670 were; (in mM) NaCl: 351.97, $MgSO_4x7H_2O$: 26.984, KCl: 9.94, NaHCO3: 2.29,
671 $MgCl_2x6H_2O$: 29.026, D-glucose: 38.08, $CaCl_2x2H_2O$: 11.38, C3H3NaO3: 5, KH_2PO_4: 0.44,
672 Na_2HP0_4: 1.34. HighK^+ Octomedia is identical to Octomedia except NaCl and KCl were
673 added as 168.65 mM and 50 mM respectively, which yielded a final concentration of 306.58
674 mM and 55.33 mM. Both solutions were adjusted to pH 7.6-7.7 with KOH, filtered using the
675 corning system (431098), stored at 4°C and used within one week. Calcium indicator CAL-
676 520 (Abcam, UK) was prepared at 5 mM in DMSO, and stored at -20°C. Dopamine, and
677 ACh were prepared at 100 µM in Octomedia. Agarose (11AGAL0050, MP Biomedicals)
678 with high gel strength (500 g/cm²) and low gelling temperature (26°C) was prepared at 3% in
679 Octomedia and kept in a 42°C water bath until ready to use.

680 **Brain dissection, embedding and sectioning**

681 1-dph paralarvae were anaesthetised in 2% ETOH/filtered artificial seawater (FASW:) until
682 motionless (at least 5 minutes). Their brains were dissected from their bodies to ensure all
683 surrounding skin/muscle were removed. The brain was then placed in the 3% agarose
684 solution in a 35mm petri dish. The agarose was left to solidify at room temperature for 5
685 minutes and then stored on ice until vibratome sectioning (within an hour). The agarose was
686 cut to a 1cm x 1cm block and sectioned with a vibrating-blade microtome (HM 650 V,
687 Thermo Scientific, UK) with the following parameters; 200 µm slice thickness, 0.2 mm/s

688 speed, and amplitude 0.7mm. The vibratome bath was filled with cooled Octomedia. Brain
689 slices were transferred to 25mm diameter circular coverslips. A temporary well was created
690 using a plastic 3D printed cylinder made from the plastic polylactic acid (10mm height, 3mm
691 wall thickness, 18mm diameter, supplemental file 6), and petroleum jelly was placed on the
692 rim of the cylinder to create a seal to the coverslip. Each slice was then incubated in CAL-
693 520 (5µM in Octomedia) for at least 1 hour at room temperature within this temporary well.
694 The cylinder was then removed and the circular coverslip containing the slice was directly
695 transferred to the imaging chamber.

696 **Calcium imaging and perfusion**

697 Imaging was performed with an upright epifluorescent microscope (Leica DM6 B) equipped
698 with a 490/525 nm excitation/emission filter set and operated at 4-5fps, which was limited by
699 exposure time (200-250 ms). The light intensity was as low as possible, dictated by a manual
700 knob on the light source. The iris was also set as low as possible to further reduce scattered
701 light and photobleaching. Perfusion inflow and compound switching were controlled by a
702 gravity valve system (Digitimer, UK), while outflow was maintained with a peristaltic pump.
703 The imaging chamber (PH2 and RC-21BDW, Science Products) was assembled with 22x40
704 mm rectangular coverslips creating a lid. The slices were immobilised using netting
705 (hexagonal pore size: 1mm x 1.5 mm) that lay on the agarose surrounding the brain slice.

706 Slices were perfused with Octomedia for 10 minutes before imaging to acclimatise the slice
707 to the imaging chamber. The perfusion protocol during imaging was as follows; Octomedia:
708 0-90s, Ligand: 90s-135s, Octomedia: 135s-270s, HighK^+ Octomedia: 270s-end:

709 **Calcium imaging analysis**

710 A total of 973 cells across 17 slices were analysed during dopaminergic stimulation in the
711 OGL of the OL. Likewise, 1090 cells over 18 slices and 2298 cells over 18 slices were

712 analysed in the IGL and medulla respectively. In terms of ACh stimulation, we analysed 391
713 cells across 12 slices from the OGL, 473 cells across 12 slices from the IGL and 858 cells
714 across 12 slices from the medulla. The calcium imaging recordings of each slice were
715 processed as follows using the Suite2p GUI[51] and a custom python
716 scripthttps://github.com/A-Courtney/Octo_Dop_ACh_Ca_Imaging_2025).

717 **Image registration**

718 We observed deformations of the tissue slice during recording sessions, likely due to
719 muscular contractions, particularly during application of the HighK^+ solution. We assume
720 that they are caused by the oesophagus that runs through the centre of the brain and perhaps
721 muscle fibres surrounding the brain that were insufficiently removed during dissection. To
722 overcome this, image registration was performed within suite2p[51] using the non-rigid
723 registration approach and 128 x 128 pixels block size
724 (https://github.com/MouseLand/suite2p).

725 **ROI detection**

726 Regions of interest (ROIs), corresponding to cells, were detected within suite2p using an
727 anatomical detection approach. This was achieved in a semi-automated way by applying the
728 cell pose 'cyto3' model to the maximum intensity projection image of each slice[50], and the
729 ROIs were then refined manually. Then within the suite2p GUI any cells that were incorrect
730 were deleted and any cells that were missing were added manually. Out of focus regions were
731 not analysed.

732 **ROI quality control**

733 The ROIs detected using the anatomical approach described above were a combination of
734 'real' cells, 'dead' cells and 'neuropil' (fluorescence signals from local neurites). Therefore,
735 we wanted to remove the 'dead' and 'neuropil' ROIs and only analyse the 'real' cell ROIs.

736 We first wanted to understand the functional characteristics of 'cellular' ROIs vs 'neuropil'
737 ROIs, we manually defined multiple ROIs using fiji[49] from five slices from different
738 paralarvae exposed to both dopamine and ACh (Supplemental Fig. 15 a-d). Manually defined
739 'cellular' ROIs had a higher fluorescence and a circular structure. Manually defined
740 'neuropil' ROIs had a lower fluorescent signal and were found in between the 'cellular'
741 ROIs. We calculated the slopes in two second windows across the full normalised fluorescent
742 trace. Slope was calculated by using the difference in fluorescence between the start and end
743 of the time window, divided by the number of frames. We observed that 'cellular' ROIs had a
744 statistically significantly higher max slope compared to 'neuropil' ROIs (t-test, $p<0.05$,
745 Supplemental Fig. 15 e). We then used the mean+standard deviation of the neuropil max
746 slope (0.0218 normalised intensity/second) as a threshold so all traces that had a max slope
747 below this are likely a heavily neuropil contaminated ROI and were removed from
748 subsequent analysis. This threshold also filtered out 'dead' ROIs as the traces from these
749 ROIs have a downward fluorescent signal over the course of the recording due to
750 photobleaching and don't show the same characteristic responses to the ligand, HighK^+
751 solution or any spontaneous activity.

752 **Defining anatomical regions**

753 To analyse the functional characteristics of cells within different regions of the optic lobe of
754 *O. vulgaris* paralarvae, we used Napari (https://github.com/napari/napari) to manually define
755 anatomical regions such as the OGL, IGL, medulla of the OL. The maximum intensity
756 projection of each slice was used to label these regions with the polygon tool.

757 **Ligand response categorisation**

758 The ligand response for each trace was defined as either excitation, inhibition or no-response.
759 Excitation was defined as the ligand stimulus window having a 20% higher mean

760 fluorescence compared to the baseline mean fluorescence (first 20 seconds of the recording),
761 when the full trace, including the HighK$^+$ response, was normalised using a min/max
762 approach (Supplemental Fig. 15 f shows example excitatory responses following dopamine
763 application. Inhibitory signals had to meet multiple criteria; 1. the ligand stimulus window
764 had to have a 20% decrease in mean fluorescence compared to the baseline mean value (first
765 20 seconds of the recording), when the full trace, including the HighK$^+$ response, was
766 normalised using a min/max approach, 2. inhibitory responses also needed to have a steep
767 downward slope (<-0.0099 normalised intensity/s) and, 3. the trough of the inhibition needed
768 to last at least 20 seconds. Supplemental Fig15 g shows example inhibitory responses
769 following ACh application. ROIs with 'no response' didn't meet either the excitation or
770 inhibition criteria and usually had a flat response during ligand application and a normal
771 HighK$^+$ response (Supplemental Fig. 15 f and g). Subtle differences in perfusion speed are
772 inevitable on different experimental days, and thus ligand and HighK$^+$ response windows
773 were manually defined.

774 **Dopamine slope analysis**

775 All dopaminergic excitatory responses that were identified above were then subsequently
776 analysed for their slope. Within each ROI trace the dopaminergic response had different onset
777 times, so the time window for calculating the dopamine response slope could not be fixed.
778 Instead, the dopamine application time window trace was extracted (80 second window),
779 smoothed using a rolling average over adjacent frames (4 second window), and normalized
780 using the min/max values. The slope is calculated as above, the time window was 2 seconds
781 and the slope for all 2 second periods across the stimulus time window were calculated, and
782 the max slope reliably identified the steepest slope of the dopaminergic response for each
783 ROI.

784 Statistical analysis of the slope of excitatory dopaminergic responses involved first checking
785 for normality per region (OGL, IGL and Med) using a Shapiro-Wilk test and none of the
786 groups were normally distributed ($p < 0.05$). The variances between the regions were not
787 equal (Levene's Test, $p < 0.05$) and thus Welch's ANOVA was used to determine if there was
788 a significant difference between the regions. Games-Howell post-hoc test was used to
789 determine which optic lobe layers had statistically significant differences in their dopamine
790 slope.

791 While only 'in-focus' cells were detected and analysed, there were still some variations in
792 how 'in-focus' a cell was. To ensure that this didn't impact our slope calculations we first
793 looked at the radius of cells, assuming cells with a larger radius were more out of focus, and
794 compared it to the slope of excitatory dopaminergic response. We performed Spearman
795 correlation and we did not observe a correlation between ROI radius and slope (R^2=-0.037,
796 p=0.0482, Supplemental Fig. 15 h). We also used variance of laplacian to calculate the
797 'sharpness' of a 30 by 30-pixel window surrounding the ROI [52] and compared it to the slope
798 of excitatory dopaminergic response. We did not observe a correlation between ROI
799 sharpness and slope (Spearman correlation, R^2=0.009, p=0.5647, Supplemental Fig. 15 i).

Figures

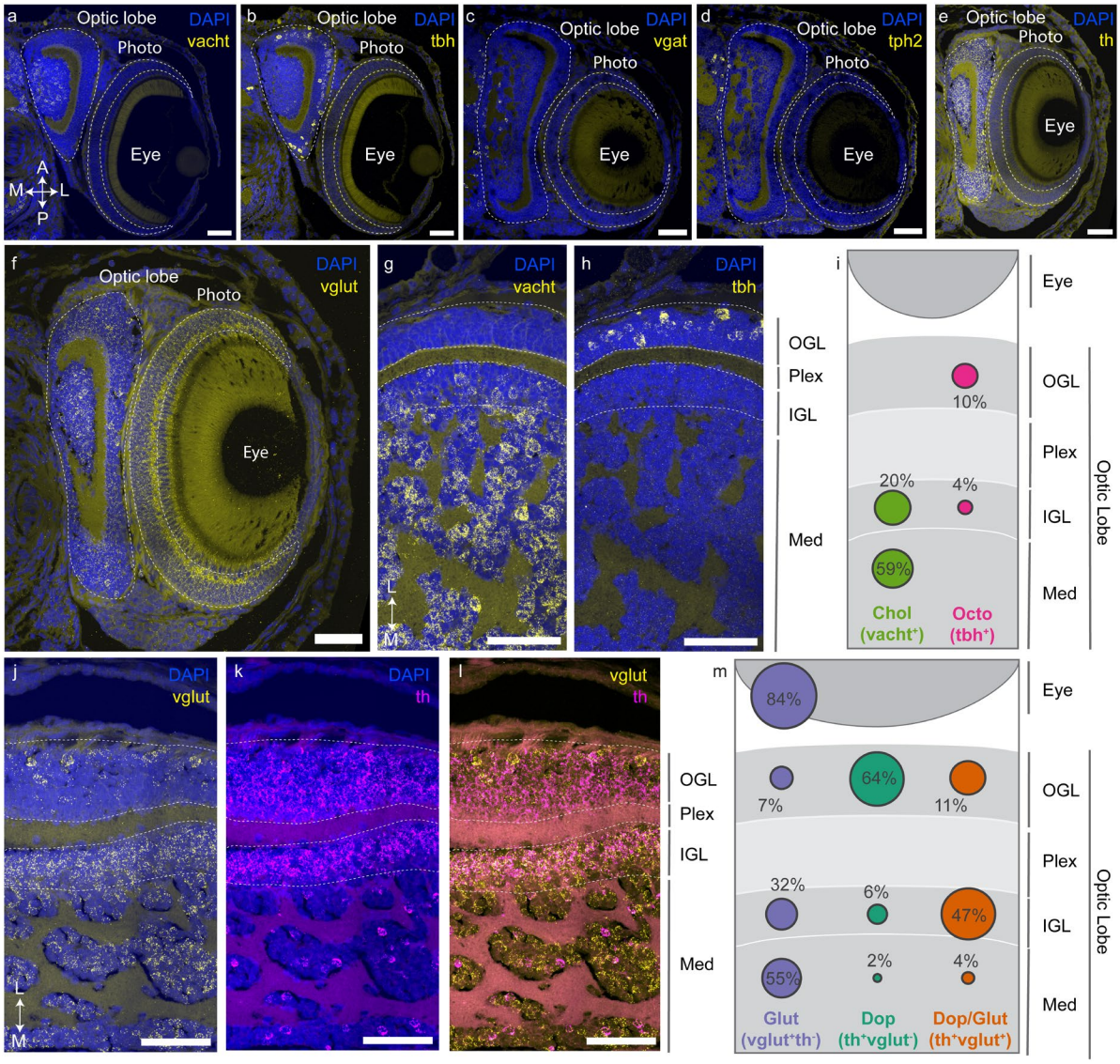

Fig. 1 Neurotransmitter cell types in the eye and optic lobe of *O. vulgaris* paralarvae. HCR was performed on 1-dph *O. vulgaris* head transversal sections; nuclei were visualised in blue with DAPI. Sections with both the optic lobe and eye visible are from the ventral (towards the arms) part of the brain (see Supplemental Fig. 7 for more details). Representative HCR against vacht (cholinergic marker) (**A** and **G**), tbh (octopaminergic marker) (**B** and **H**), vgat (GABAergic marker) (**C**), tph2 (serotonergic marker) (**D**), th (dopaminergic marker) (**E** and **K**), and vglut (glutamatergic marker) (**F** and **J)** in yellow. Representative multiplex HCR against th (dopaminergic cell marker) in magenta and vglut (glutamatergic cell marker) in yellow (**L**). Summary of HCR analysis of Chol and Octo cell types in the eye and optic lobe (**I**). Summary of HCR analysis of Glut, Dop and Dop/Glut cell types in the eye and optic lobe (**M)** The size of the circle represents the proportion of cells in

813 that layer belonging to that cell type. The head orientation is the same in A to F, G to M.
814 Scale bar: 50 µm. vacht: vesicular acetylcholine transporter, tbh: tyramine beta hydroxylase,
815 vgat: vesicular GABA transporter, tph2: tryptophan hydroxylase, th: tyrosine hydroxylase,
816 vglut: vesicular glutamate transporter, OGL: outer granular layer, IGL: inner granular layer,
817 Med: medulla, Plex: plexiform layer, Octo: octopaminergic cell type (tbh^+), Chol: cholinergic
818 cell type ($vacht^+$), Dop: exclusively dopaminergic cell type (th^+vglut^-), Glut: exclusively
819 glutamatergic cell type ($vglut^+/th^-$), Dop/Glut: exclusively dopaminergic and glutamatergic
820 cell type (th^+vglut^+), A: anterior, P: posterior, M: medial, L: lateral.
821

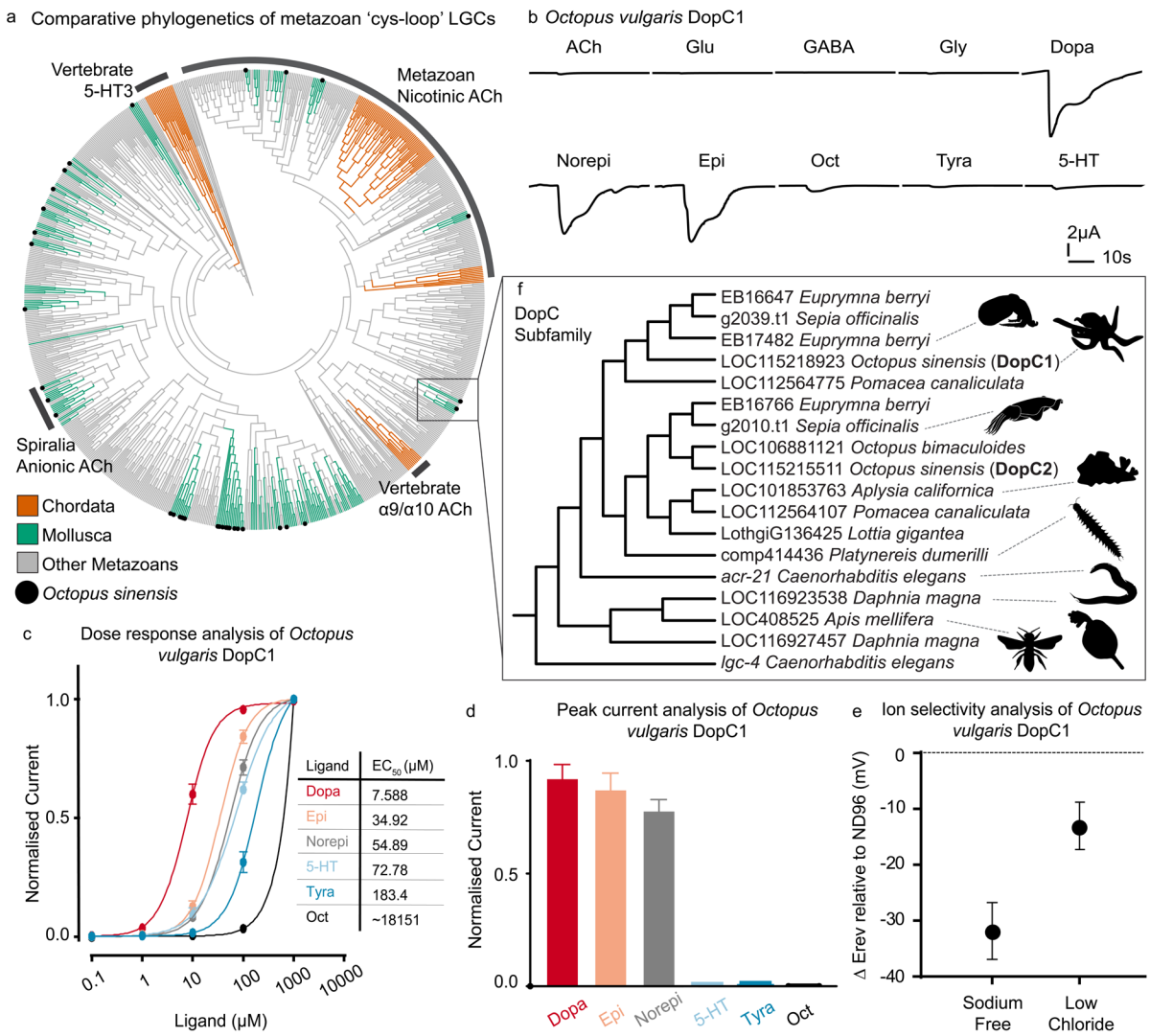

Fig. 2 A dopamine-gated cation channel in *Octopus vulgaris* and other invertebrates (**A**) Comparative phylogenetics of nicotinic-like cys-loop ligand gated ion channels from major metazoan phyla (cys-less and GABA-A like branches were collapsed). Chordata sequences are highlighted in orange and molluscan sequences are highlighted in green. *Octopus sinensis* sequences are highlighted with a black dot. A zoomed view of the DopC1 subfamily is in panel (**F**). (**B**). Representative TEVC traces from *Xenopus* oocytes expressing DopC1 from *O. vulgaris* during application of candidate ligands. ACh: acetylcholine, Glu: glutamate, Gly: glycine, Dopa: dopamine, Norepi: norepinephrine, Epi: epinephrine, Oct: octopamine, Tyra: tyramine, and 5-HT: serotonin. (**C**). Monoamine dose response analysis curves for *O. vulgaris* DopC1 expressed in *Xenopus* oocytes. The adjacent table includes the EC_{50} values for each ligand in μM. Mean and standard error are plotted for 3-7 separate oocytes per ligand. The current was normalised to the max current in each oocyte. (**D**). Peak current analysis (mean and standard deviation) of *O. vulgaris* DopC1 expressed in *Xenopus*

836 oocytes. Each oocyte was exposed to 1 mM of the indicated monoamine. The current was
837 normalised to the peak current in each oocyte. (**E**). Ion selectivity analysis of *O. vulgaris*
838 DopC1 expressed in *Xenopus* oocytes during TEVC recordings Plotted is the difference in
839 reversal potential (Erev, in mV) of the channel, measured during activation with 10µM
840 (~EC_{50}) dopamine between ND96 and the sodium-free solution or the low-chloride solution.
841 The mean and standard deviation are shown for 5 oocytes.
842

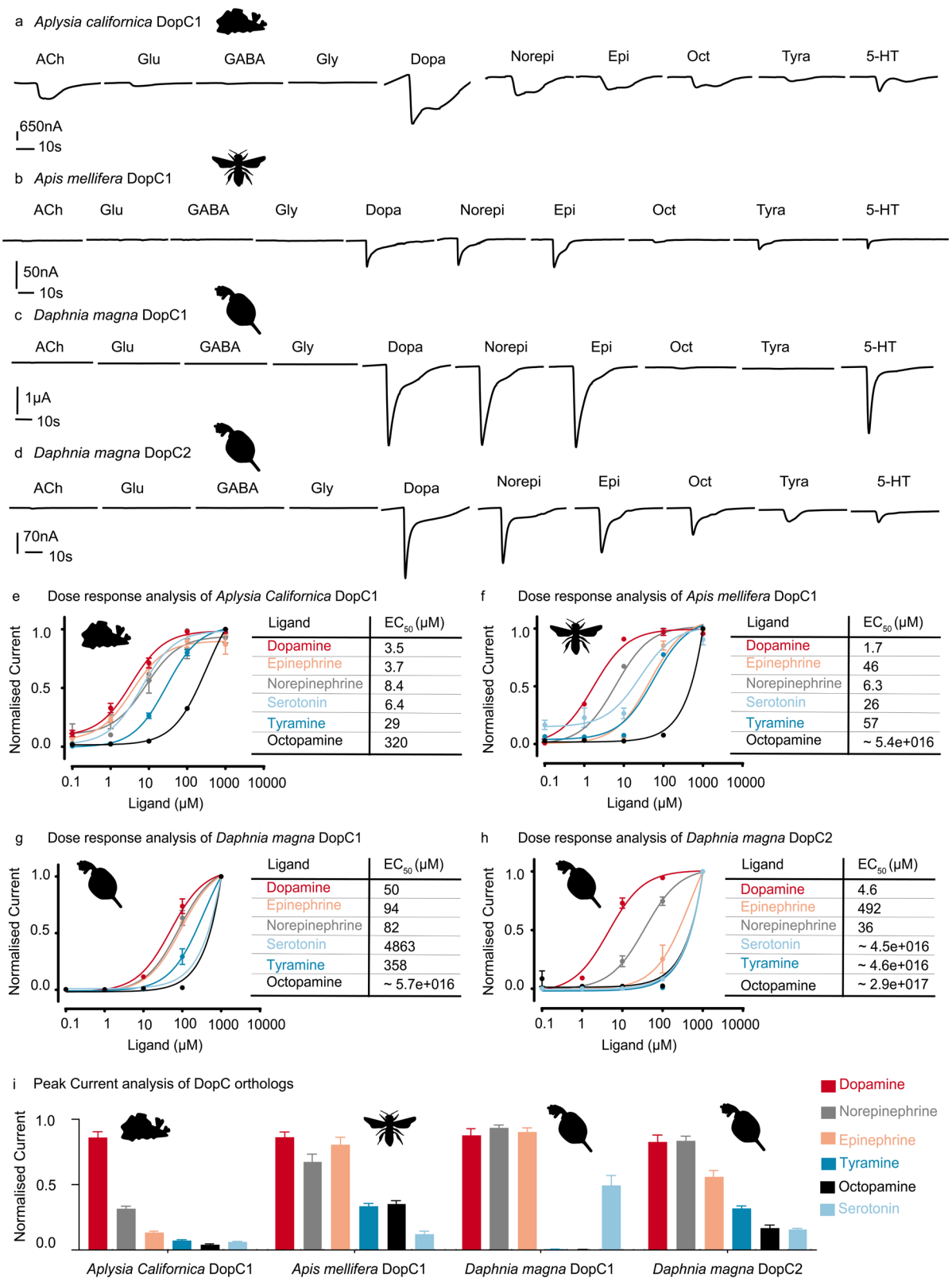

Fig. 3 Functional characterisation of DopC orthologs from *Aplysia californica, Apis mellifera* and *Daphnia magna.*

847 Representative TEVC traces from *Xenopus* oocytes expressing DopC1 from *Aplysia*
848 *californica* (**A**), DopC1 from *Apis mellifera* (**B**), DopC1 from *Daphnia magna* (**C**), and
849 DopC2 from *Daphnia magna* (**D**) during application of candidate ligands. Dose response
850 analysis curves for the major monoamines during TEVC recordings of *Xenopus* oocytes
851 expressing DopC1 from *Aplysia californica* (**E**), DopC1 from *Apis mellifera* (**F**), DopC1
852 from *Daphnia magna* (**G**), DopC2 from *Daphnia magna* (**H**). The adjacent table includes the
853 EC_{50} values for each ligand in µM. Mean and standard error are plotted for 3-7 separate
854 oocytes per ligand. The current was normalised to the max current in each oocyte. Peak
855 current analysis for homomeric DopC orthologs from *Aplysia californica*, *Apis mellifera* and
856 *Daphnia magna* expressed in *Xenopus* oocytes (**I**). During TEVC recordings each oocyte was
857 exposed to 1mM dopamine, epinephrine, norepinephrine, serotonin, tyramine and
858 octopamine. The mean and standard error of the mean are plotted per ligand, per receptor.
859 The current has been normalised to the peak current in each oocyte. ACh: acetylcholine, Glu:
860 glutamate, Gly: glycine, Dopa: dopamine, Norepi: norepinephrine, Epi: epinephrine, Oct:
861 octopamine, Tyra: tyramine, 5-HT: serotonin, DopC: dopamine-gated cation channel.
862

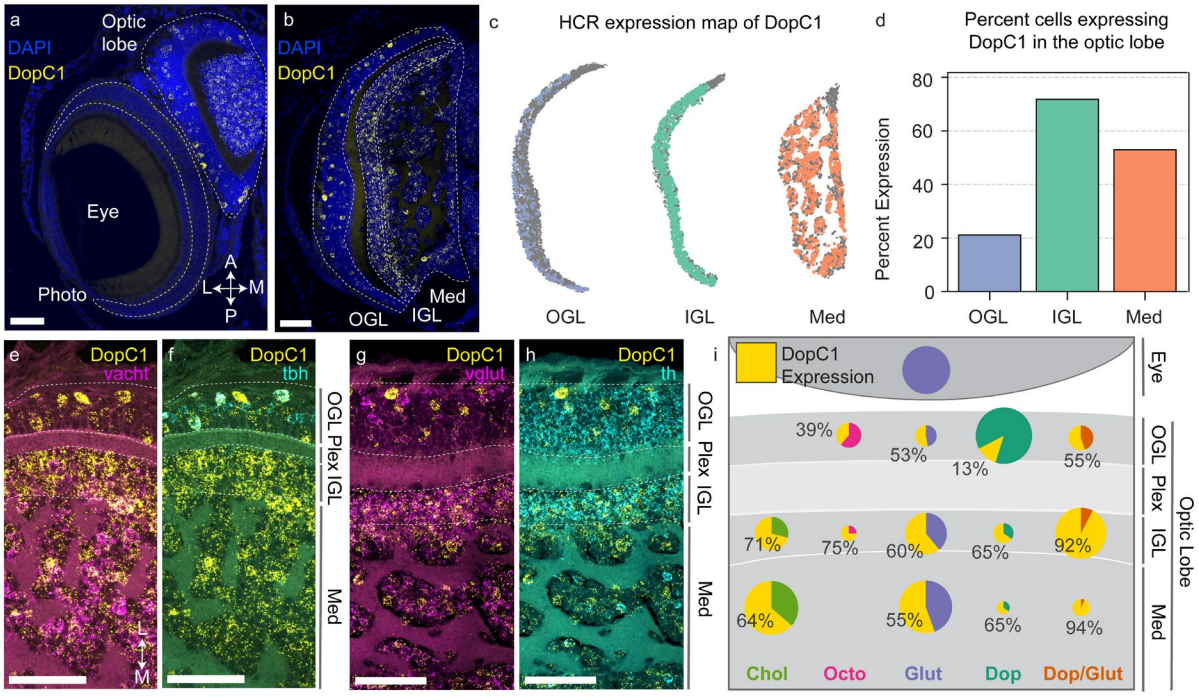

Fig. 4 DopC1 expression in the eye and optic lobe of *O. vulgaris* 1dph paralarvae.

(**A** and **B**) Representative hybridisation chain reaction (HCR) analysis of DopC1 expression. HCR was performed on 1-dph *O. vulgaris* head transversal sections; DopC1-expressing cells are in yellow; nuclei were visualised in blue with DAPI. (**C** and **D**) HCR expression maps (**C**) and barplot (**D**) showing the proportion and spatial distribution of cells expressing DopC1 in the OGL, IGL and Med of the OL, quantified from the HCR shown in B. (**E-H**) Representative multiplex HCR against DopC1 and indicated neurotransmitter markers. DopC1 is in yellow (all panels); vacht (cholinergic cell marker) in magenta (**E**), tbh (octopaminergic cell marker) in cyan (**F**), vglut (glutamatergic cell marker) in magenta (**G**) and th (dopaminergic cell marker) in cyan (**H**). The head orientation in A-C and E-I is the same. Scale bar: 50 µm. A: anterior, P: posterior, M: medial, L: lateral. (**I**) Summary of the expression of DopC1 in the major neurotransmitter cell types in the eye and OL. OGL: outer granular layer, IGL: inner granular layer, Med: medulla, Plex: plexiform layer, Octo: octopaminergic cell type (tbh^{+}), Chol: cholinergic cell type (vacht^{+}), Dop: exclusively dopaminergic cell type (th^{+}vglut^{-}), Glut: exclusively glutamatergic cell type (vglut^{+}/th^{-}), Dop/Glut: dopaminergic and glutamatergic cell type (th^{+}vglut^{+}). The size of the circle representatives the proportion of cells in that layer that belong to that cell type; the yellow sector represents the proportion of cells of that cell type that express DopC1. This quantification was performed on the multiplex HCRs shown in Supplemental Fig. 6.

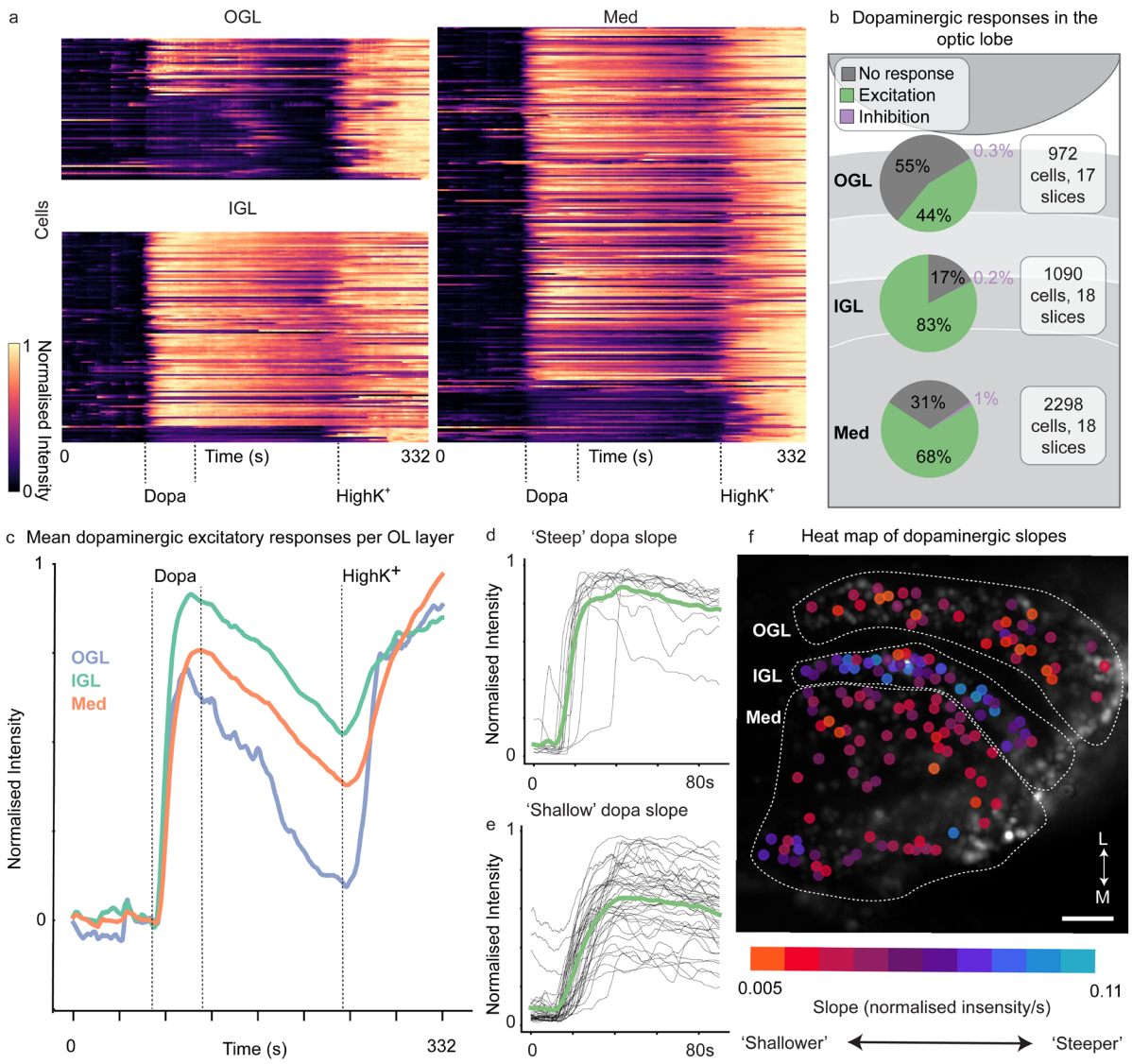

Fig. 5 Dopamine excites neural activity in *O. vulgaris* paralarvae acute brain slices.

(**A**). Calcium imaging was performed on 1-dph *O. vulgaris* acute brain slices during application of 100 µM dopamine (Dopa) and the HighK$^+$ solution. Shown is a heat map of a representative slice during calcium imaging, with lines corresponding to individual cells in the indicated layer. The fluorescence intensity for each ROI was smoothed using a rolling average window over 10 seconds and normalised using min/max values per ROI. (**B**) Pie charts showing the proportion of cells which have dopaminergic excitation, dopaminergic inhibition or no response to dopamine, within the different layers of the optic lobe, summed across all brain slices (**C**). Mean traces from the representative slice shown in A per optic lobe layer (**D**). A subset of dopaminergic responses with 'steep' slopes (>0.075 normalised intensity/s) were characterised as fast-rising responses (**E**). A subset of dopaminergic excitatory responses with "shallow" slopes (between 0.0125 and 0.0375 normalised

896 intensity/s) were classes as slower responses. For responses in D and E, the mean trace is
897 shown in green. (**F**). Maximum intensity projection of a representative brain slice with
898 coloured dots indicating the slope values of the excitatory dopaminergic responses in the
899 different layers of the optic lobe. 'Steep', fast-rising responses were most prevalent in the
900 IGL, where DopC1 is most extensively expressed. Scale bar: 50 µm;, M: medial, L: lateral.

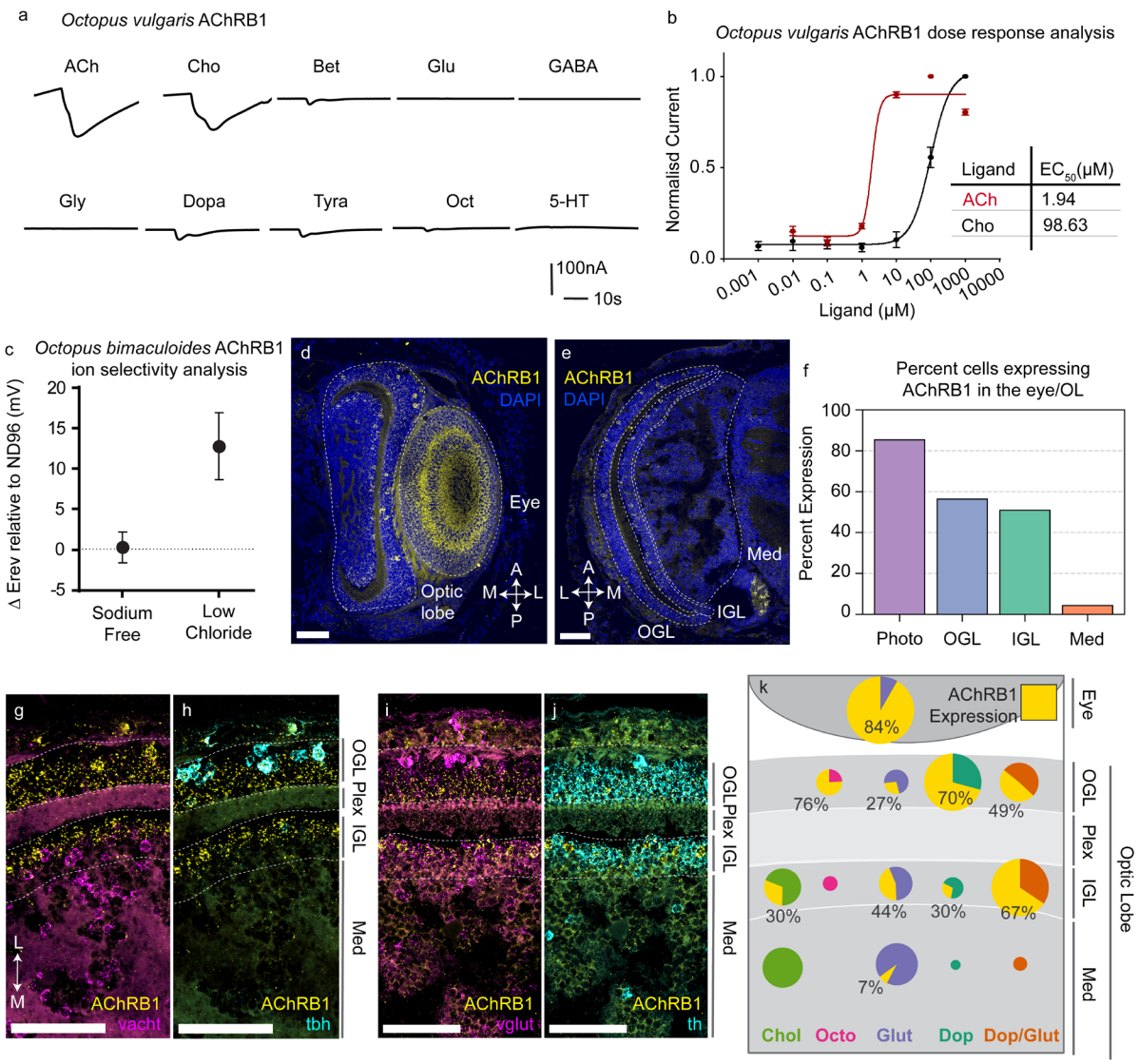

Fig. 6 AChRB1, an ACh-gated chloride channel expressed in the *O. vulgaris* visual system

(**A**) Representative traces from *Xenopus* oocytes expressing *O. vulgaris* AChRB1 upon application of candidate ligands. Ligand abbreviations are as in Fig 2. (**B**) Dose response curves for ACh and choline for *O. vulgaris* AChRB1 expressed in *Xenopus* oocytes. EC_{50} values for each ligand are shown in the table. Mean and standard error are plotted for 5-6 separate oocytes per ligand; the current was normalised to the max current in each oocyte. (**C**) Ion selectivity analysis of *O. bimaculoides* AChRB1 expressed in *Xenopus* oocytes. Plotted is the difference in reversal potential (Erev, in mV) of the channel upon activation with 1μM ACh (~EC_{50}) between ND96 and either sodium-free solution or low-chloride solution. The mean and standard deviation are shown for 7 oocytes. (**D** and **E**) Representative HCR analysis of AChRB1 expression. All HCRs were performed on 1-dph *O. vulgaris* head

914 transversal sections; AChRB1-expressing cells are in yellow, nuclei were visualised in blue
915 with DAPI. (**F**) Barplot showing the proportion of cells expressing AChRB1 in the eye and
916 OL, quantified from the HCR shown in D and E (**G-J**) Representative multiplex HCR against
917 AChRB1 and indicated neurotransmitter markers; AChRB1 is in yellow (all panels); vacht
918 (cholinergic cell marker) in magenta (**G**), tbh (octopaminergic cell marker) in cyan (**H**), vglut
919 (glutamatergic cell marker) in magenta (**I**) and th (dopaminergic cell marker) in cyan (**J**). The
920 orientation in all panels is the same; scale bar: 50 µm. (**K**) Summary of AChRB1 expression
921 of AChRB1 in the eye and OL. Cell type and layer abbreviations are as in Fig 1. The size of
922 the circle represents the proportion of cells in that layer that belong to that cell type; the
923 yellow sector represents the proportion of cells of that neurotransmitter type that also express
924 AChRB1. This quantification was performed on the multiplex HCRs shown in Supplemental
925 Fig. 11.

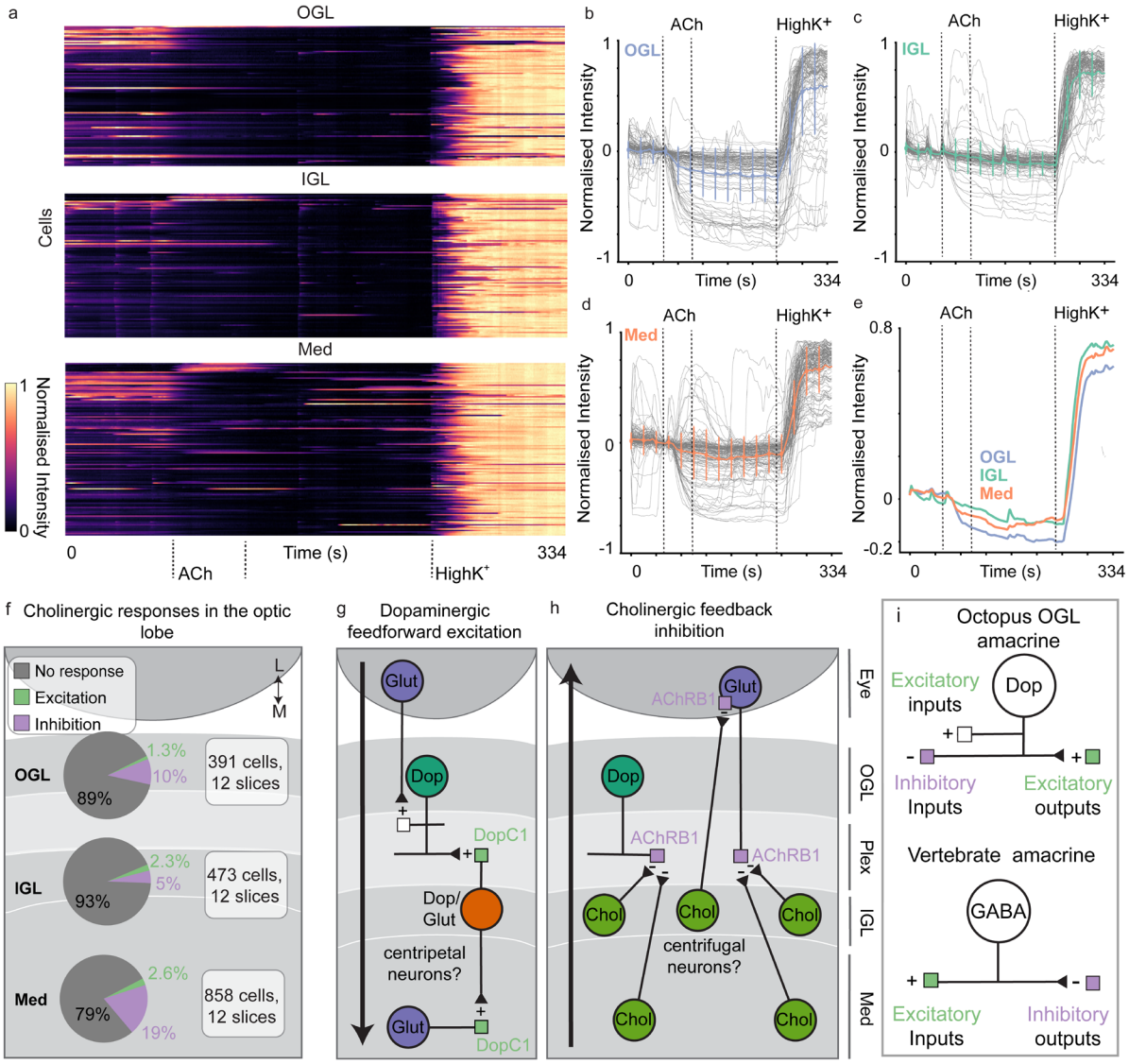

926

927 **Fig. 7 Acetylcholine inhibits neural activity in *O. vulgaris* paralarval acute brain slices**
928 (**A**) Calcium imaging was performed on 1-dph *O. vulgaris* acute brain slices during
929 application of 100 µM ACh (ACh) and the HighK$^+$ solution. Shown are heat maps of a
930 representative brain slice, with lines corresponding to individual cells in the indicated layer.
931 The fluorescence intensity for each ROI was smoothed using a rolling average window over
932 10 second periods and normalised using min/max values per ROI. **(B-E)** Normalised intensity
933 over time for all ROIs of the representative slice in panel A in the OGL (**B**), IGL (**C**) and
934 Med (**D**). Mean trace and error bars are highlighted in bold. Panel **E** shows the mean traces
935 from B-D overlayed on each other (**F**). Pie charts showing the proportion of cells which
936 showed excitation, inhibition or no response to ACh, within the different layers of the OL,
937 summed across all brain slices (**G-I**). Circuit hypotheses. Cell type and layer abbreviations
938 are as in Fig 1. (**G**) Dopamine is hypothesises do carry out feedforward excitation between

939 the OGL and IGL, and between IGL and Med. (**H**) Acetylcholine is hypothesised to carry out
940 feedback inhibition between the IGL and/or Med and the OGL and/or photoreceptors. (**I**).
941 Differences in input and output valences between octopus OGL dopaminergic amacrine cells
942 and vertebrate retinal GABAergic amacrine cells.
943

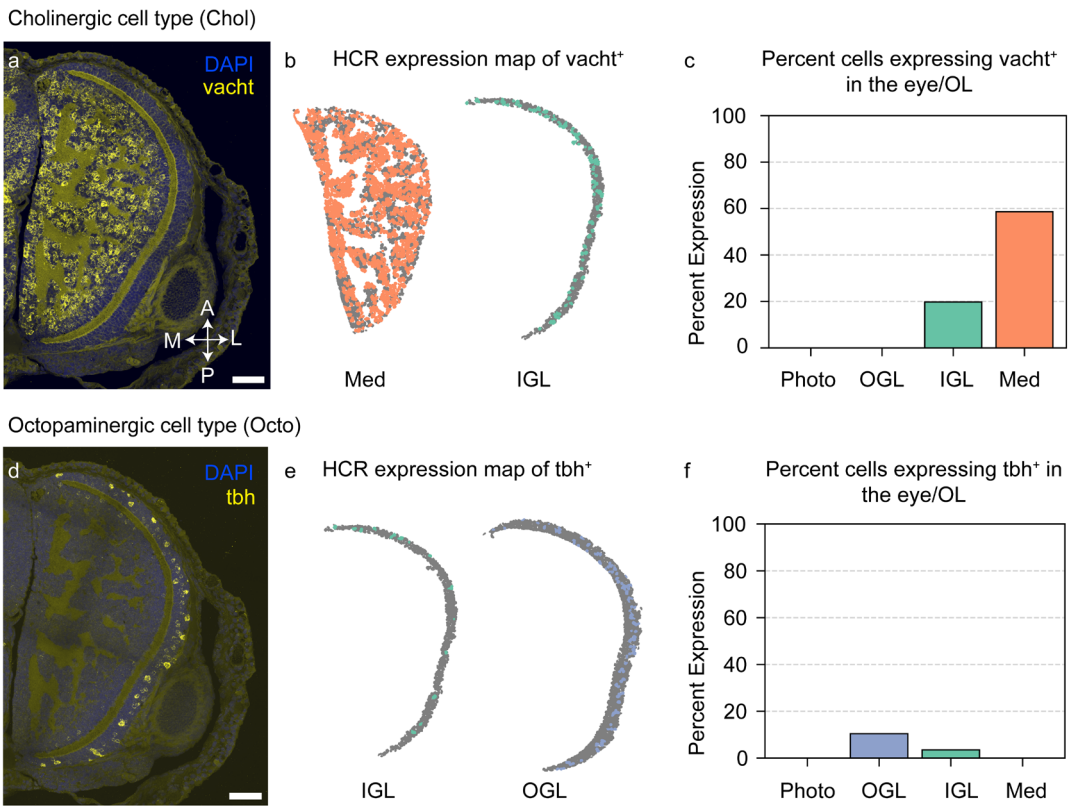

Supp Fig. 1 Quantitative and spatial analysis of Chol and Octo cell types in the visual system of 1-dph O. vulgaris paralarvae.

HCRs were performed on 1-dph *O. vulgaris* head transversal sections and nuclei are visualised in blue with DAPI. (**A**). Representative HCR against vacht (cholinergic cell marker) in yellow. A custom python script was used to quantify the expression pattern for each gene of interest within nuclear regions in the eye and optic lobe (see methods). (**B-D**) HCR expression maps (**B**) and barplot (**C**) showing the proportion and spatial distribution of cells expressing vacht in the eye/OL, quantified from the HCR shown in A. (**D**). Representative HCR against tbh (octopaminergic cell marker) in yellow (**E-F**) HCR expression maps (**E**) and barplot (**F**) showing the proportion and spatial distribution of cells expressing tbh in the eye/OL, quantified from the HCR shown in D. The orientation in A and D are the same. Scale bar: 50 µm, vacht: vesicular acetylcholine transporter, tbh: tyramine beta hydroxylase, Photo: photoreceptors, OGL: outer granular layer, IGL: inner granular layer, Med: medulla, OL: optic lobe, Octo: octopaminergic cell type (tbh^{+}), Chol: cholinergic cell type (vacht^{+}), A: anterior, P: posterior, M: medial, L: lateral.

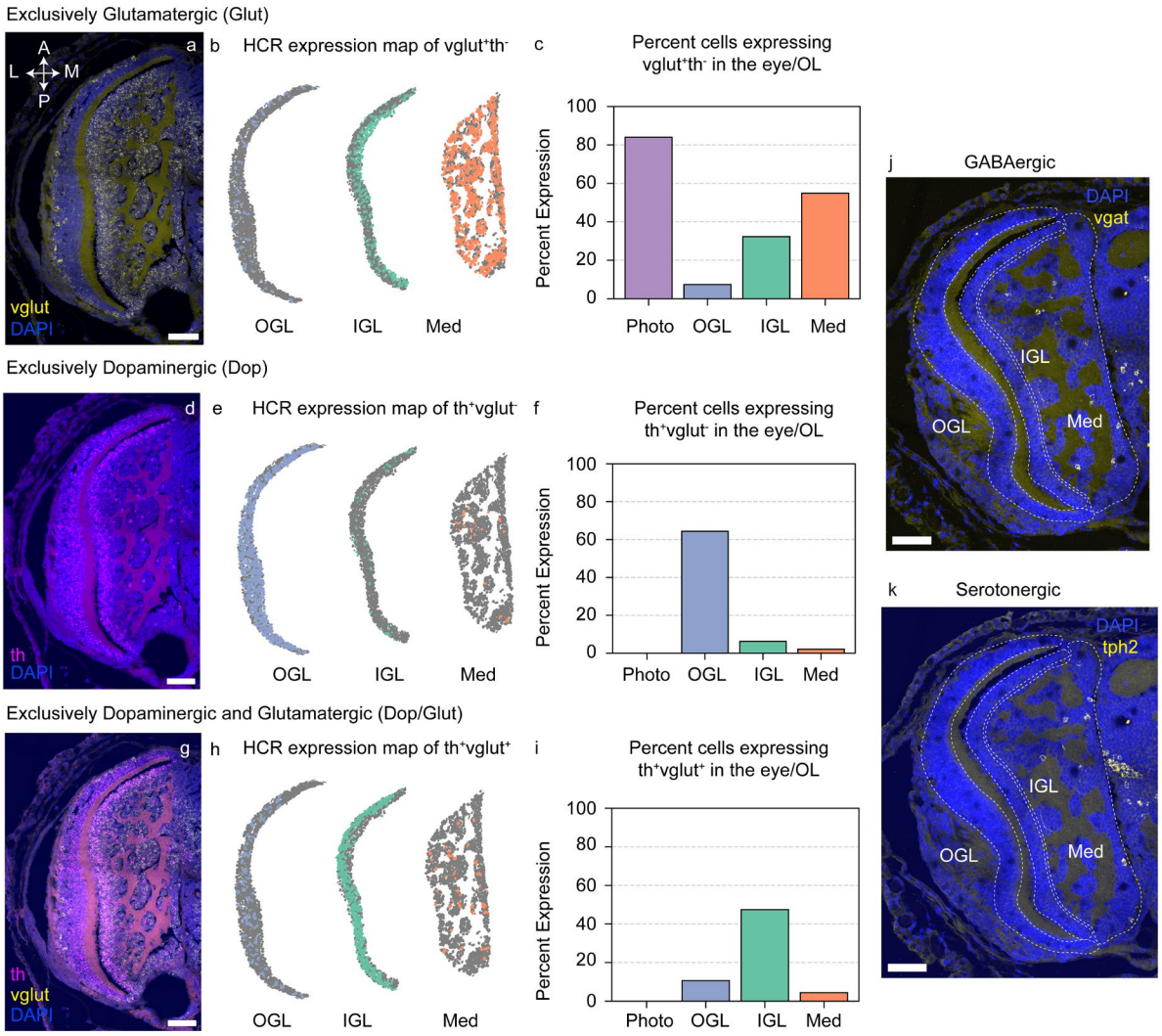

Supp Fig. 2 Quantitative and spatial analysis of Glut, Dop and Dop/Glut cell types in the visual system

All HCRs were performed on 1-dph *O. vulgaris* head transversal sections; nuclei were visualised in blue with DAPI. (**A**) Representative HCR against the glutamatergic marker vglut (vesicular glutamate transporter) is shown in yellow. A custom python script was used to quantify the expression pattern for each gene of interest within nuclear regions in the eye and optic lobe (see methods). HCR expression maps (**B**) and barplot (**C**) show the proportion and spatial distribution of cells expressing vglut exclusively ($vglut^{+}th^{-}$) in the eye/OL, quantified from the HCR shown in A. (**D**) Representative HCR against dopaminergic marker th (tyrosine hydroxylase) in magenta. HCR expression maps (**E**) and barplot (**F**) show the proportion and spatial distribution of cells expressing th exclusively ($th^{+}vglut^{-}$) in the eye/OL, quantified from the HCR shown in D. (**G**) Representative HCR against both th (in magenta) and vglut (in yellow). HCR expression maps (**H**) and barplot (**I**) show the proportion of

975 Dop/Glut cells (th^+vglut^+) in the eye/OL, quantified from the HCR shown in G. (**I-K**)
976 Representative HCR against GABAergic marker vgat (vesicular GABA transporter) (**J**) and
977 serotonergic cell marker tph2 (tryptophan hydroxylase) (**K**) in yellow. All HCRs have the
978 same orientation. Scale bar: 50 µm, vgat:, tph2:, th: tyrosine hydroxylase, vglut:, Photo:
979 photoreceptors, OGL: outer granular layer, IGL: inner granular layer, Med: medulla, OL:
980 optic lobe, Dop: exclusively dopaminergic cell type (th^+vglut^-), Glut: exclusively
981 glutamatergic cell type ($vglut^+/th^-$), Dop/Glut: dopaminergic and glutamatergic cell type
982 (th^+vglut^+), A: anterior, P: posterior, M: medial, L: lateral.
983

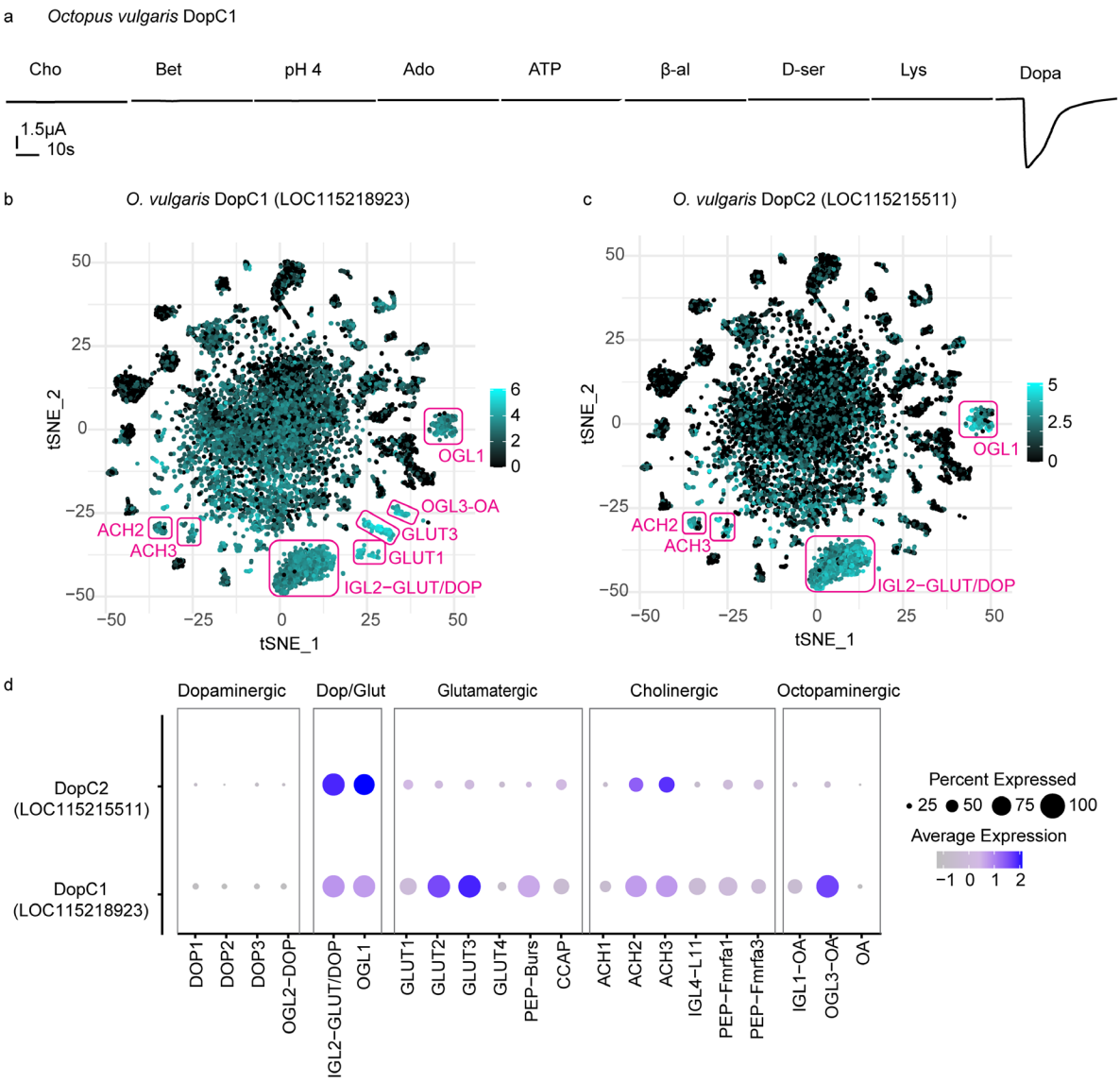

Supp Fig. 3 Additional functional and expression analysis of DopC1 from *O. vulgaris*

(**A**) Representative TEVC traces from *Xenopus* oocytes expressing DopC1 from *O. vulgaris* during application of additional candidate ligands. (**B-C**) tSNE of scRNA-seq of the *O. vulgaris* paralarval brain[9], showing the expression of the DopC1 (LOC115218923) (**B**) and DopC2 (LOC115215511) (**C**). All clusters that show high expression are highlighted in magenta. (**D**) Dot plot of a subset of clusters from the single cell RNAseq of the *O. vulgaris* paralarval brain showing the expression of DopC1 and DopC2. The size of the dots relates to the percent of cells in that cluster that express the gene, the heat map corresponds to the average expression of the gene in all cells in the cluster. Cho: choline, Bet: betaine, Ado: adenosine, ATP: adenosine triphosphate, β-al: β-alanine, Lys: lysine, Dopa: dopamine.

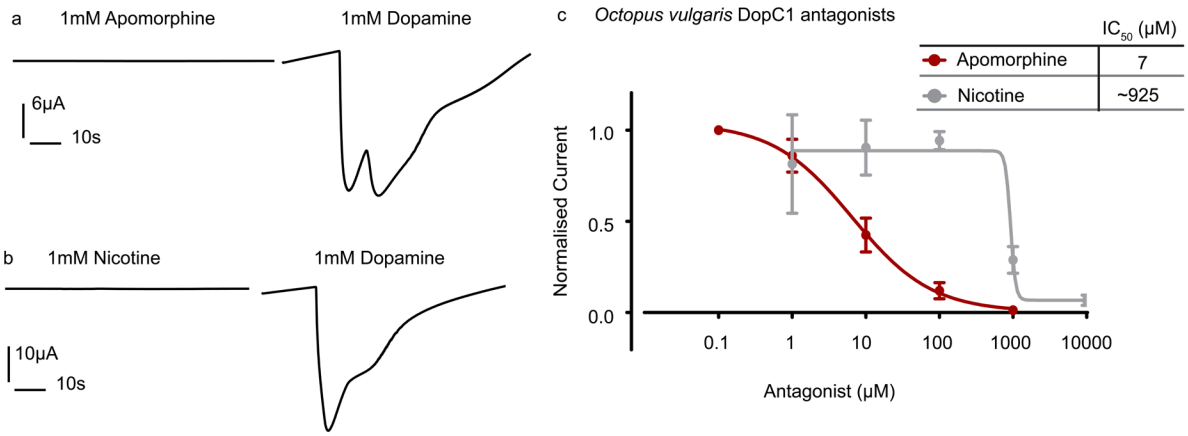

Supp Fig. 4 Characterising Octopus vulgaris DopC1 candidate agonists and antagonists (**A-B**) Representative TEVC traces from *Xenopus* oocytes expressing *O. vulgaris* DopC1 during application of apomorphine (**A**) and nicotine (**B**). (**C**) Antagonist inhibitory dose response curves from *Xenopus* oocytes expressing DopC1 from *O. vulgaris*. This was acquired by applying low to high doses of each antagonist in the presence of dopamine at 10μM (~EC_{50}). The adjacent table includes the IC_{50} values for each ligand in μM. Mean and standard error are plotted for 5-7 independent oocytes per antagonist. The current was normalised to the max current in each oocyte.

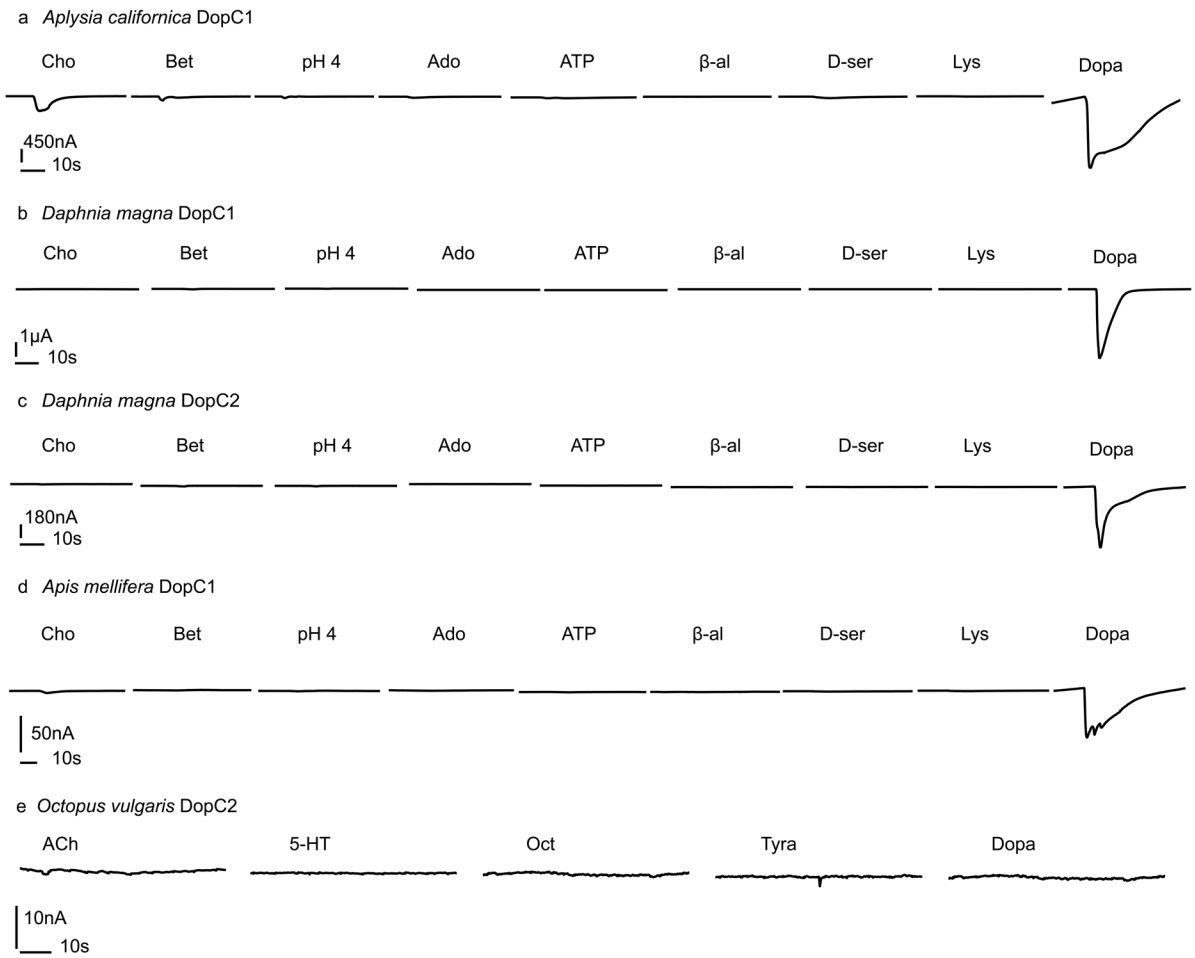

Supp Fig. 5 Functional characterization of DopC orthologs from *Aplysia californica, Apis mellifera* and *Daphnia magna*

Representative TEVC traces from *Xenopus* oocytes expressing DopC1 from *Aplysia californica* (**A**), DopC1 from *Daphnia magna* (**B**), DopC2 from *Daphnia magna* (**C**), DopC1 from *Apis mellifera* (**D**) and DopC2 from *Octopus vulgaris* (**E**) during application of candidate ligands. ACh: acetylcholine, Cho: choline, Bet: betaine, Ado: adenosine, ATP: adenosine triphosphate, β-al: β-alanine, D-ser: D-serine, Lys: lysine, Dopa: dopamine, Oct: octopamine, Tyra: tyramine, 5-HT: serotonin, DopC: dopamine-gated cation channel.

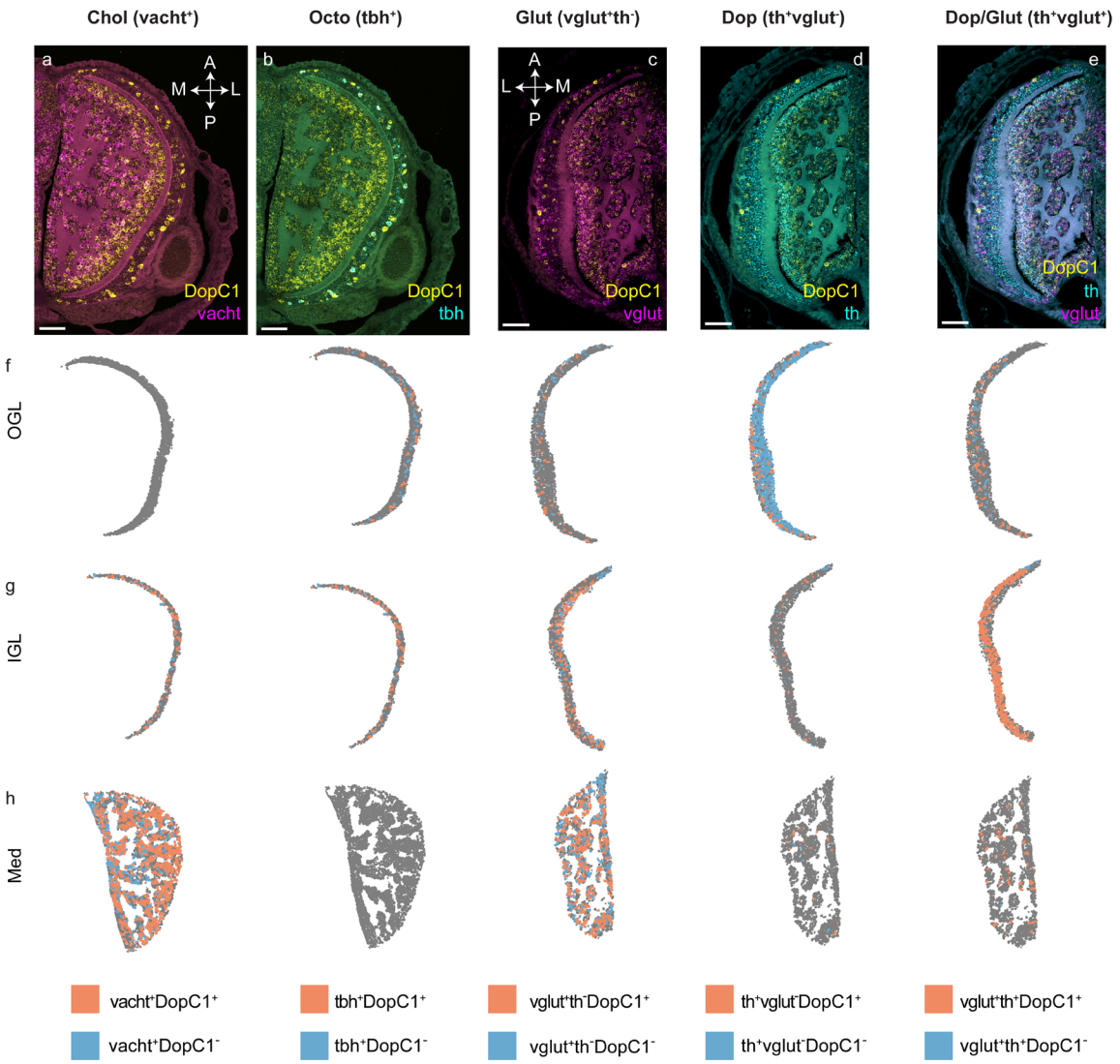

1020

1021 **Supp Fig. 6 Quantitative and spatial analysis of DopC1 expression in the brain of *O.***
1022 ***vulgaris***
1023 Representative multiplex HCR against DopC1 in yellow and vacht (cholinergic marker) in
1024 magenta (**A**), tbh (octopaminergic marker) in cyan (**B**), vglut (glutamatergic marker) in
1025 magenta (**C**) and th (dopaminergic marker) in cyan (**D**). (**C** and **E**) Representative multiplex
1026 HCR against DopC1 in yellow, vglut (glutamatergic cell marker) in magenta (**C**) and th
1027 (dopaminergic cell marker) in cyan (**E**). (**F-H**) Representative HCR expression maps of Chol,
1028 Octo, Glut, Dop and Dop/Glut cell types in the OGL (**F**), IGL (**G**) and Med (**H**) of the OL,
1029 with cells positive for DopC1 in orange and those negative for DopC1 in blue. The
1030 expression maps were quantified from the HCRs shown above and the results are summarised
1031 in Fig. 4 i. The orientation in A and B and C-D are the same. Cell type, layer, and gene names
1032 are as described in previous figures. Scale bar: 50 µm.

1033

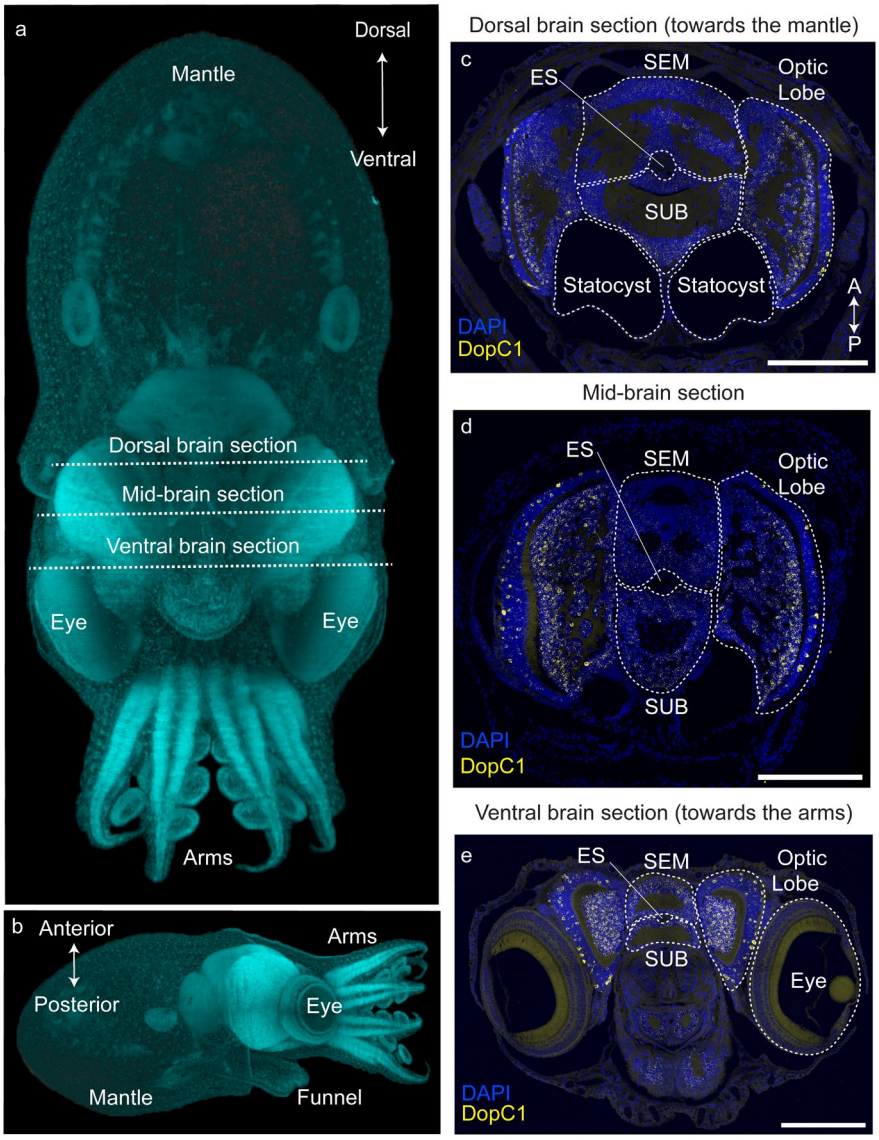

Supp Fig. 7 DopC1 expression in the central brain of *O. vulgaris* paralarvae

(**A** and **B**) Maximum intensity projection of DAPI labelled 1-dph *O. vulgaris* paralarva imaged with light sheet microscopy, reproduced with permission from Deryckere et al.[53]. (**C-E**) Representative HCR against DopC1 in yellow and nuclei (DAPI) in blue, at a dorsal position of the brain (towards the mantle) (**C**), at a mid position of the brain (**D**) and at a ventral position of the brain (towards the arms) (**E**). Scale bar: 200µm, SEM: supraesophageal mass of the central brain, SUB: subesophageal mass of the central brain, ES: oesophagus, A: anterior, P: posterior.

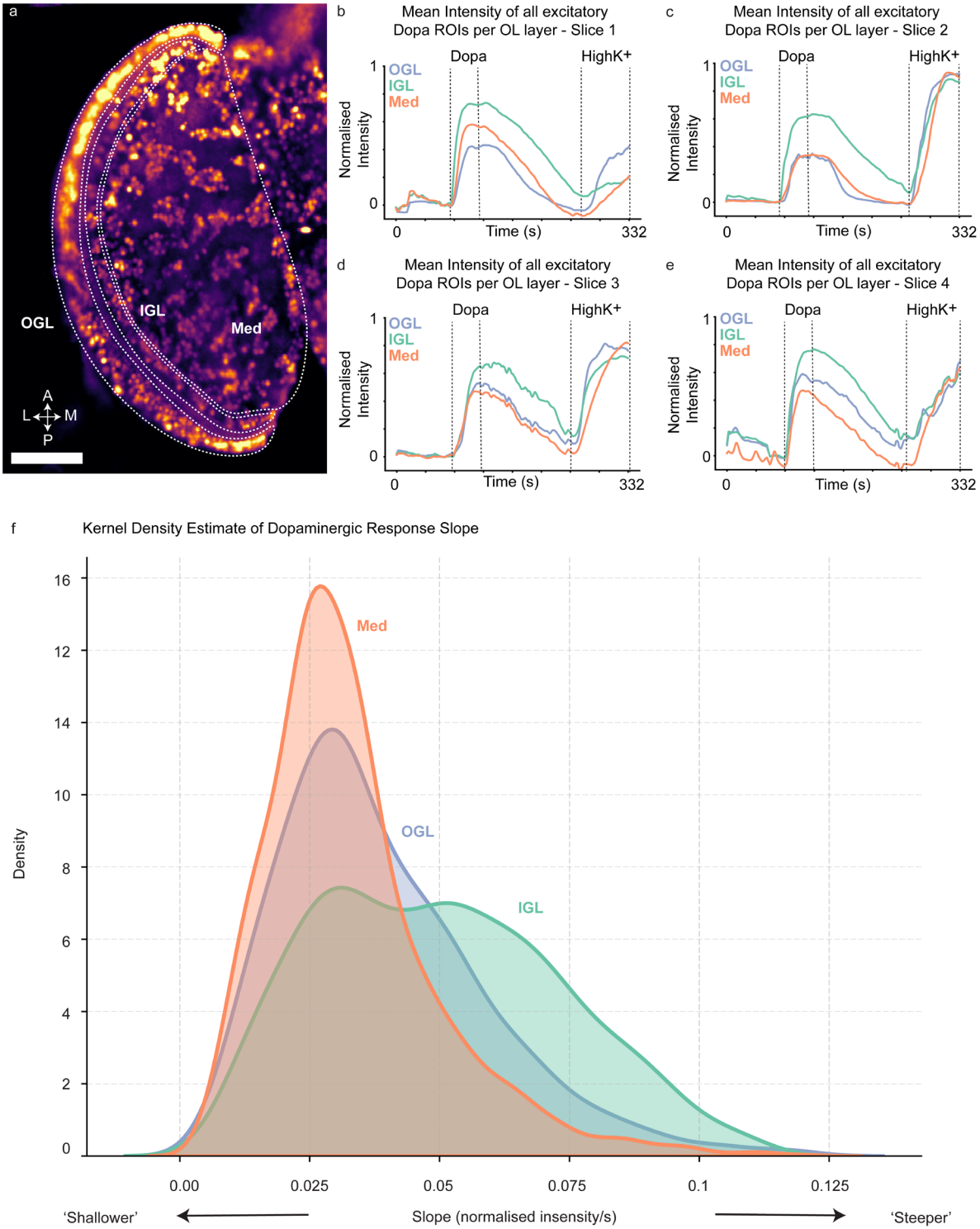

Supp Fig. 8 Additional analysis of calcium imaging on acute brain slices from *O. vulgaris* paralarvae during application of dopamine

Calcium imaging was performed on acute brain slices from 1-dph *O. vulgaris* paralarvae. (**A**) Maximum intensity projection of a representative brain slice used for calcium imaging. (**B-E**) The mean intensity over time for all ROIs in each optic lobe layer that were categorised as having an excitatory dopaminergic response are plotted as purple (OGL), green (IGL) and

1051 orange (Med) lines. Four different slices have been plotted. (**F**) Kernel density estimate of
1052 dopaminergic response slope per optic lobe layer. Scale bar: 100 µm, Dopa: dopamine,
1053 HighK^+: high potassium solution, OGL: outer granular layer, IGL: inner granular layer, Med:
1054 medulla, A: anterior, P: posterior, M: medial, L: lateral.

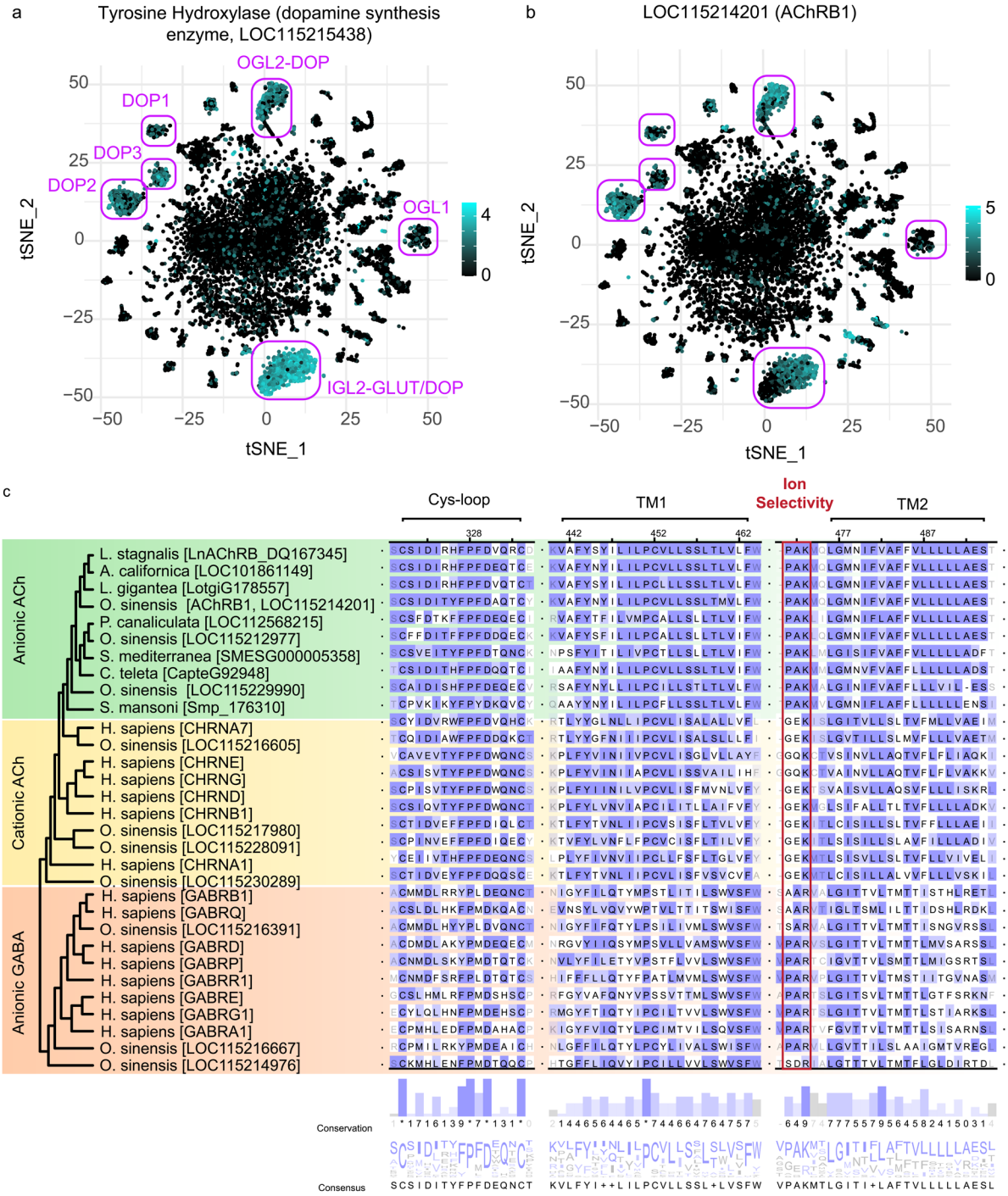

Supp Fig. 9 Additional expression, and sequence analysis of AChRB1 from *O. vulgaris*

tSNE of scRNA-seq of the *O. vulgaris* paralarval brain from[9], showing the expression of dopaminergic marker th (tyrosine hydroxylase, LOC115215438) (**A**) and AChRB1 (LOC115214201) (**B**). Dopaminergic clusters are highlighted in magenta. Trimmed amino acid alignment showing a subset of anionic ACh, cationic ACh and anionic GABA LGCs highlighting multiple functional domains including the cys-loop region, transmembrane domain 1, the ion selectivity region and transmembrane domain 2 (**C**). Amino acid consensus

1063 and conservation values are shown below. Purple shading indicates BLOSUM62 scores
1064 indicating evolutionary divergence of individual sites. TM: transmembrane,
1065

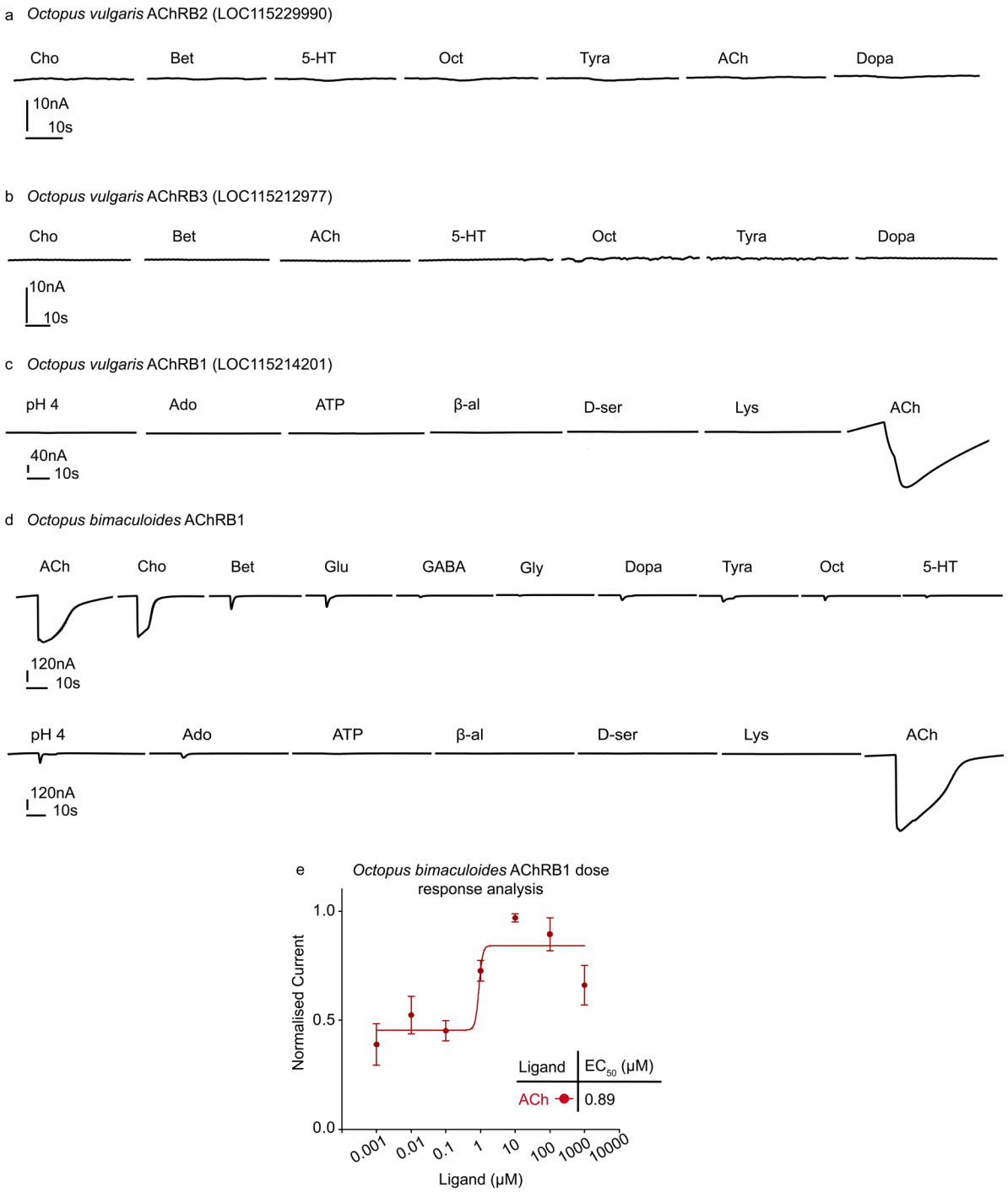

1066

1067 **Supp Fig. 10 Functional characterisation of AChRB orthologs from *O. vulgaris* and *O.***
1068 ***bimaculoides***

1069 Representative TEVC traces from *Xenopus* oocytes expressing *O. vulgaris* AChRB2 (**A**), *O.*
1070 *vulgaris* AChRB3 (**B**), *O. vulgaris* AChRB1 (**C**), and *O. bimaculodes* AChRB1(**D**) during
1071 application of all candidate ligands. For D the top and bottom traces were from separate
1072 oocytes. (**E**) Dose response analysis curves for *O. bimaculoides* AChRB1 in response to

1073 ACh. This was acquired by performing TEVC recordings on *O. bimaculoides AChRB1*
1074 expressed in *Xenopus* oocytes from low to high concentrations. The adjacent table indicates
1075 the EC_{50} values for ACh in μM. Mean and standard error of the mean are plotted for 8
1076 separate oocytes per ligand. The current was normalised to the max current in each oocyte.
1077 ACh: acetylcholine, Chol: choline, Bet: betaine, Glut: glutamate, Gly: glycine, Ado:
1078 adenosine, ATP: adenosine triphosphate, β-al: β-alanine, Lys: lysine, Dop: dopamine, Norepi:
1079 norepinephrine, Epi: epinephrine, Octo: octopamine, Tyra: tyramine, 5-HT: serotonin.
1080

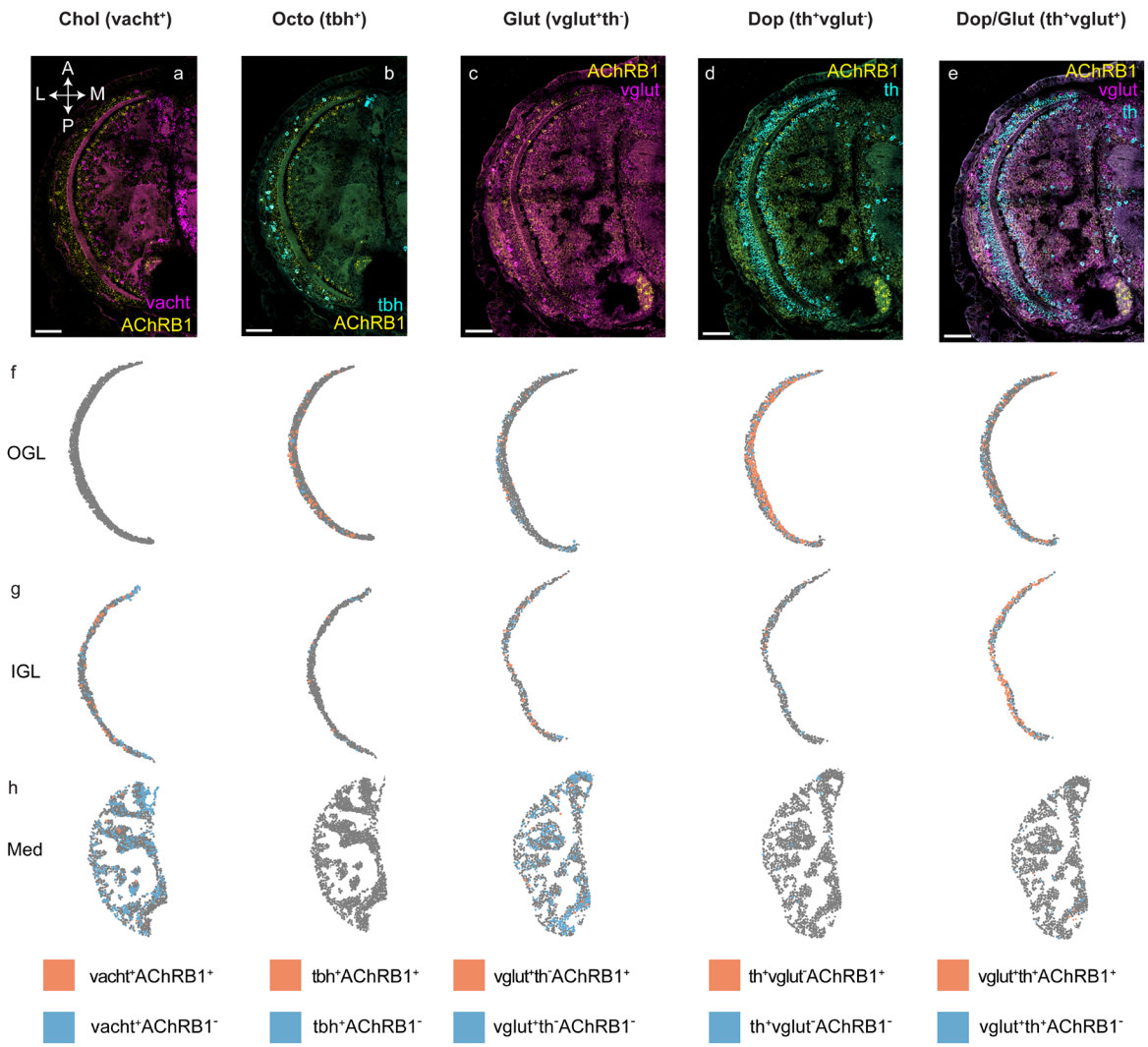

Supp Fig. 11 Quantitative and spatial analysis of AChRB1 expression in the brain of *O. vulgaris*.

HCRs were performed on 1-dph *O. vulgaris* head transversal sections. Representative multiplex HCR against AChRB in yellow and vacht (cholinergic marker) in magenta (**A**), tbh (octopaminergic marker) in cyan (**B**), vglut (glutamatergic marker) in magenta (**C**) and th (dopaminergic marker) in cyan (**D**). (**C** and **E**) Representative multiplex HCR against AChRB in yellow, vglut (glutamatergic marker) in magenta (**C**) and th (dopaminergic marker) in cyan (**E**). (**F-H**) Representative HCR expression maps of Chol, Octo, Glut, Dop and Dop/Glut cell types in the OGL (**F**), IGL (**G**) and Med (**H**) of the OL, with cells positive for AChRB1 in orange) and those negative for AChRB1 in blue. The expression maps were quantified from the HCRs shown above and the results are summarised in Fig. 6 k. The

1093 orientation of all HCRs is the same. Cell type, layer, and gene names are as described in
1094 previous figures. Scale bar: 50 µm.

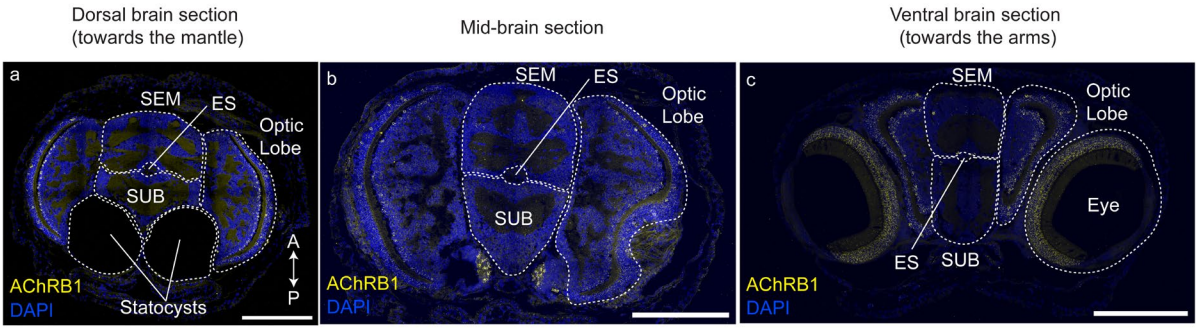

1095

1096 **Supp Fig. 12 AChRB1 expression in the central brain of *O. vulgaris* paralarvae**
1097 Representative HCR against AChRB1 in yellow and nuclei (DAPI) in blue, at a dorsal
1098 position of the brain (towards the mantle) (**A**), at a mid-brain position (**B**) and at a ventral
1099 brain position (towards the arms) (**C**). For more details on ventral/dorsal orientations of the
1100 paralarvae see Supplemental Fig. 8. Scale bars: 200µm, SEM: supraesophageal mass of the
1101 central brain, SUB: subesophageal mass of the central brain, ES: oesophagus.

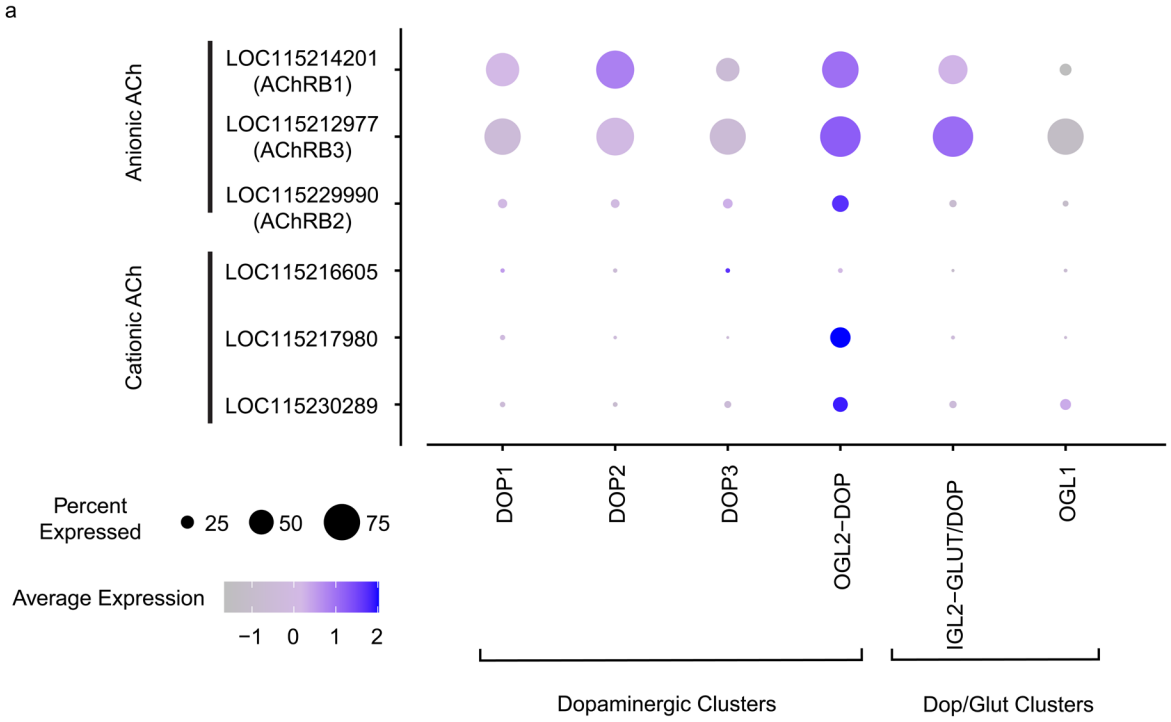

Supp Fig. 13 Expression analysis of anionic and cationic ACh-gated channels in dopaminergic and Dop/Glut cells

Dot plot of exclusively dopaminergic and Dop/Glut clusters from the scRNA-seq of the *O. vulgaris* paralarval brain[9], showing the expression of anionic and cationic ACh genes. The size of the dots relates to the percent of cells in that cluster that express the gene, the heat map corresponds to the average expression of the gene in all cells in the cluster.

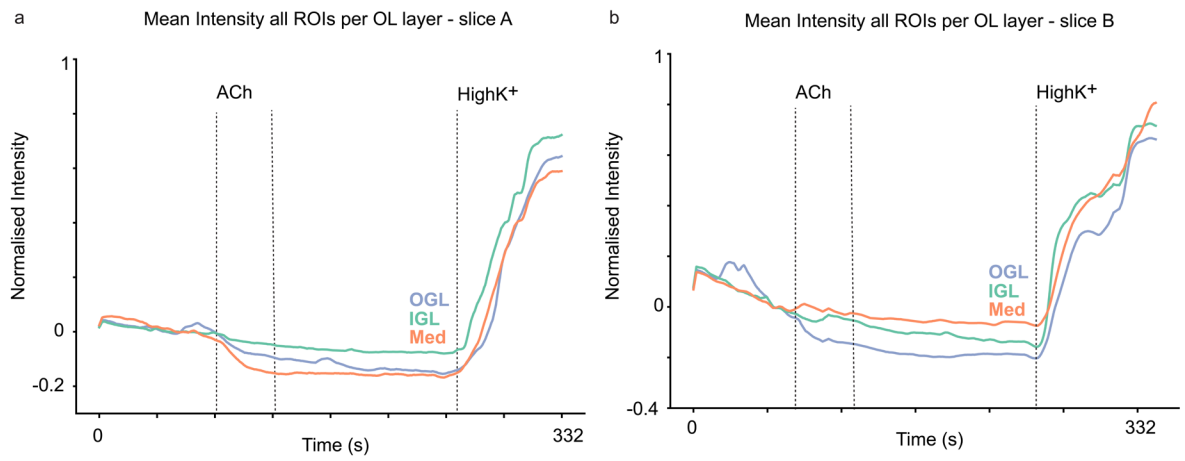

Supp Fig. 14 Additional analysis of calcium imaging on acute brain slices from O. vulgaris paralarvae during application of ACh

Calcium imaging was performed on acute brain slices from 1-dph *O. vulgaris* paralarvae during application of 100 µM ACh and HighK$^+$. The mean intensity over time for all ROIs in each optic lobe layer are plotted as purple (OGL), green (IGL) and orange (Med) lines. Two different slices have been plotted (**A** and **B**). HighK$^+$: high potassium solution, ACh: acetylcholine, OGL: outer granular layer, IGL: inner granular layer, Med: medulla.

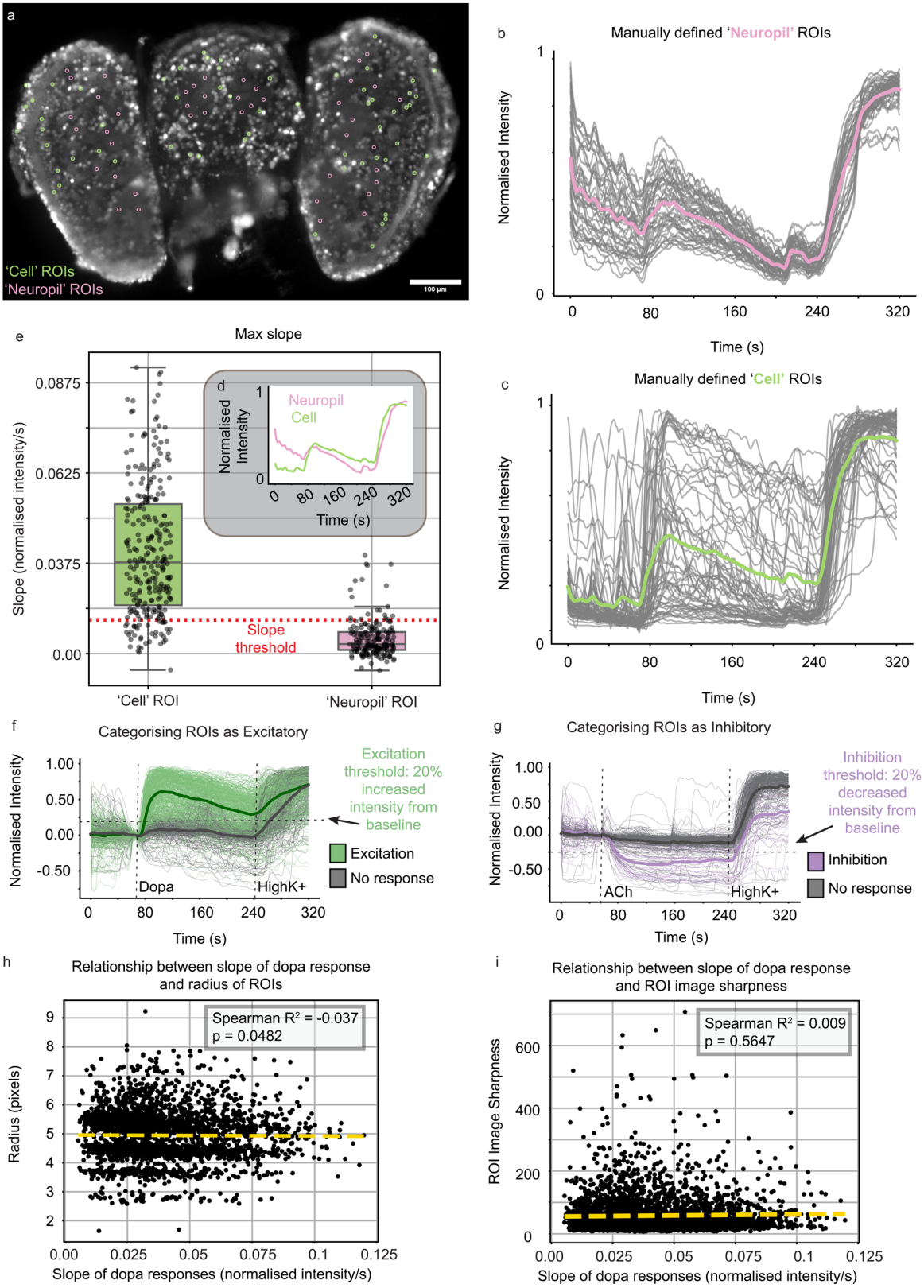

Supp Fig. 15 Calcium imaging methodology

Calcium imaging was performed on acute brain slices from 1-dph *O. vulgaris* paralarvae. Maximum intensity projection of a representative brain slice used for calcium imaging with manually defined ROIs for 'Neuropil' (pink) and 'Cells' (green) (**A**). Normalised mean

1139 intensity over time for all manually defined 'Neuropil' ROIs from A in grey. Mean trace is
1140 represented in pink (**B**). Normalised mean intensity over time for all manually defined 'Cell'
1141 ROIs from A in grey. Mean trace is represented in green (**C**). Mean 'Neuropil' and 'Cell'
1142 ROIs from B and C overlayed (**D**) The max slope was calculated for all manually defined
1143 'Cell' and 'Neuropil' ROIs from five slices from five different paralarvae used for calcium
1144 imaging (**E**). The red dotted line is the mean + standard deviation of the 'Neuropil' ROI max
1145 slope. The normalised intensity of all traces from a representative slice that was exposed to
1146 100 µM dopamine and HighK$^+$ (**F**). The traces that were categorised as 'excitation' are in
1147 green and the traces that were categorised as 'no response' are in grey. The mean trace for
1148 each group is highlighted as a thicker grey or green trace. The normalised intensity of all
1149 traces from a representative slice that was exposed to 100 µM ACh and HighK$^+$ (**G**). The
1150 traces that were categorised as 'inhibition' are in purple and the traces that were categorised
1151 as 'no response' are in grey. The mean trace for each group is highlighted as a thicker grey or
1152 green trace. A scatter plot comparing the relationship between the radius of a cell ROI (**H**) or
1153 the sharpness of the image surrounding a ROI (**I**) and the slope of excitatory dopaminergic
1154 responses. The results of a Spearman correlation test are seen as a dotted yellow line. Scale
1155 bar: 100 µm, Dopa: dopamine, ACh: acetylcholine, HighK$^+$: high potassium solution, ROI:
1156 region of interest.

Supplemental files

Supplemental file 1 – names and gene IDs for all receptors functionally characterised in this study.

Supplemental file 2 – citations for all receptors included in the phylogenetic tree which had a functional annotation.

Supplemental file 3 – protein sequence alignment for 'cys-loop' LGCs from major metazoan phyla.

Supplemental file 4 – full phylogenetic tree for 'cys-loop' LGCs from major metazoan phyla. All receptors that have been previously functionally characterised have their ligand highlighted in yellow.

Supplemental file 5 – list of HCR probes used in this study.

Supplemental file 6 – stl file for 3D printed cylinder used as a temporary well during calcium imaging experiments.

Bibliography

1 Young, J. Z. THE NUMBER AND SIZES OF NERVE CELLS IN OCTOPUS. *Proceedings of the Zoological Society of London* **140**, 229-254 (1963). https://doi.org:https://doi.org/10.1111/j.1469-7998.1963.tb01862.x

2 Kverková, K. *et al.* The evolution of brain neuron numbers in amniotes. *Proceedings of the National Academy of Sciences* **119**, e2121624119 (2022). https://doi.org:10.1073/pnas.2121624119

3 Hochner, B., Shomrat, T. & Fiorito, G. The octopus: a model for a comparative analysis of the evolution of learning and memory mechanisms. *The Biological bulletin* **210**, 308-317 (2006). https://doi.org:10.2307/4134567

4 Vitti, J. J. Cephalopod Cognition in an Evolutionary Context: Implications for Ethology. *Biosemiotics* **6**, 393-401 (2013). https://doi.org:10.1007/s12304-013-9175-7

5 Pungor, J. R. & Niell, C. M. The neural basis of visual processing and behavior in cephalopods. *Current Biology* **33**, R1106-R1118 (2023). https://doi.org:https://doi.org/10.1016/j.cub.2023.08.093

6 Young, J. Z. The optic lobes of Octopus vulgaris. *Philosophical transactions of the Royal Society of London. Series B, Biological sciences* **245**, 19-58 (1962).

7 Pungor, J. R., Allen, V. A., Songco-Casey, J. O. & Niell, C. M. Functional organization of visual responses in the octopus optic lobe. *Current Biology* **33**, 2784-2793.e2783 (2023). https://doi.org:10.1016/j.cub.2023.05.069

8 Demb, J. B. & Singer, J. H. Functional Circuitry of the Retina. *Annual Review of Vision Science* **1**, 263-289 (2015). https://doi.org:https://doi.org/10.1146/annurev-vision-082114-035334

9 Styfhals, R. *et al.* Cell type diversity in a developing octopus brain. *Nature communications* **13**, 7392 (2022). https://doi.org:10.1038/s41467-022-35198-1

10 Songco-Casey, J. O. *et al.* Cell types and molecular architecture of the Octopus bimaculoides visual system. *Current Biology* **32**, 5031-5044.e5034 (2022). https://doi.org:https://doi.org/10.1016/j.cub.2022.10.015

11 Lam, D. M. K., Wiesel, T. N. & Kaneko, A. Neurotransmitter synthesis in cephalopod retina. *Brain research* **82**, 365-368 (1974). https://doi.org:https://doi.org/10.1016/0006-8993(74)90621-0

12 Piscopo, S. *et al.* Pre- and postsynaptic excitation and inhibition at octopus optic lobe photoreceptor terminals; implications for the function of the 'presynaptic bags'. *The European journal of neuroscience* **26**, 2196-2203 (2007). https://doi.org:10.1111/j.1460-9568.2007.05833.x

13 Chrachri, A. & Williamson, R. Dopamine modulates synaptic activity in the optic lobes of cuttlefish, Sepia officinalis. *Neuroscience letters* **377**, 152-157 (2005). https://doi.org:10.1016/j.neulet.2004.11.089

14 Gisselmann, G., Pusch, H., Hovemann, B. T. & Hatt, H. Two cDNAs coding for histamine-gated ion channels in D. melanogaster. *Nature neuroscience* **5**, 11-12 (2002). https://doi.org:10.1038/nn787

15 Ringstad, N., Abe, N. & Horvitz, H. R. Ligand-gated chloride channels are receptors for biogenic amines in C. elegans. *Science* **325**, 96-100 (2009). https://doi.org:10.1126/science.1169243

16 Morud, J. *et al.* Deorphanization of novel biogenic amine-gated ion channels identifies a new serotonin receptor for learning. *Current biology : CB* (2021). https://doi.org:10.1016/j.cub.2021.07.036

17 Hardege, I., Morud, J., Courtney, A. & Schafer, W. R. A Novel and Functionally Diverse Class of Acetylcholine-Gated Ion Channels. *The Journal of neuroscience : the official journal of the Society for Neuroscience* **43**, 1111-1124 (2023). https://doi.org:10.1523/JNEUROSCI.1516-22.2022

18 Nixon, M. & Mangold, K. The early life of Octopus vulgaris (Cephalopoda: Octopodidae) in the plankton and at settlement: a change in lifestyle. *Journal of Zoology* **239**, 301-327 (1996).

19 Giuditta, A., Libonati, M., Packard, A. & Prozzo, N. Nuclear counts in the brain lobes ofoctopus vulgaris as a function of body size. *Brain research* **25**, 55-62 (1971).

20 Elagoz, A. M., Van Dijck, M., Lassnig, M. & Seuntjens, E. Embryonic development of a centralised brain in coleoid cephalopods. *Neural development* **19**, 8 (2024). https://doi.org:10.1186/s13064-024-00186-2

21 Villanueva, R. & Norman, M. D. in *Oceanography and marine biology* 111-208 (CRC Press, 2008).

22 Lees, A. J. Dopamine agonists in Parkinson's disease: a look at apomorphine. *Fundamental & Clinical Pharmacology* **7**, 121-128 (1993). https://doi.org:https://doi.org/10.1111/j.1472-8206.1993.tb00226.x

23 van Nierop, P. *et al.* Identification of Molluscan Nicotinic Acetylcholine Receptor (nAChR) Subunits Involved in Formation of Cation- and Anion-Selective nAChRs. *The Journal of Neuroscience* **25**, 10617 (2005). https://doi.org:10.1523/JNEUROSCI.2015-05.2005

24 MacDonald, K. *et al.* Functional Characterization of a Novel Family of Acetylcholine-Gated Chloride Channels in Schistosoma mansoni. *PLOS Pathogens* **10**, e1004181 (2014). https://doi.org:10.1371/journal.ppat.1004181

25 Jensen, M. L., Schousboe, A. & Ahring, P. K. Charge selectivity of the Cys-loop family of ligand-gated ion channels. *Journal of neurochemistry* **92**, 217-225 (2005). https://doi.org:10.1111/j.1471-4159.2004.02883.x

26 Young, J. Z. *The anatomy of the nervous system of Octopus vulgaris*. (Clarendon Press, 1971).

27 Green, K. A. & Cottrell, G. A. Dopamine directly activates a ligand-gated channel in snail neurones. *Pflügers Archiv* **431**, 639-644 (1996). https://doi.org:10.1007/BF02191914

28 Ranganathan, R., Cannon, S. C. & Horvitz, H. R. MOD-1 is a serotonin-gated chloride channel that modulates locomotory behaviour in C. elegans. *Nature* **408**, 470-475 (2000). https://doi.org:10.1038/35044083

29 Gavriouchkina, D. *et al.* A single-cell atlas of the bobtail squid visual and nervous system highlights molecular principles of convergent evolution. *Nature Ecology & Evolution* **9**, 1245-1262 (2025). https://doi.org:10.1038/s41559-025-02720-9

30 Rencken, S. *et al.* Chromosome-scale genome assembly of the European common cuttlefish <em>Sepia officinalis</em&gt. *bioRxiv*, 2025.2004.2022.649952 (2025). https://doi.org:10.1101/2025.04.22.649952

31 Norton, A. C., Fukada, Y., Motokawa, K. & Tasaki, K. An investigation of the lateral spread of potentials in the octopus retina. *Vision Research* **5**, 253-267 (1965). https://doi.org:https://doi.org/10.1016/0042-6989(65)90003-9

32 Piscopo, S. *et al.* Pre- and postsynaptic excitation and inhibition at octopus optic lobe photoreceptor terminals; implications for the function of the 'presynaptic bags'. *European Journal of Neuroscience* **26**, 2196-2203 (2007). https://doi.org:https://doi.org/10.1111/j.1460-9568.2007.05833.x

33 Almansa, E. *et al.* in *Aquaculture and Living Resource Management – Volume 2* (ed P.L. Pereira) (CRC Press (Taylor & Francis Group), 2025).

34 Destanović, D. *et al.* A chromosome-level reference genome for the common octopus, Octopus vulgaris (Cuvier, 1797). *G3 Genes|Genomes|Genetics* **13**, jkad220 (2023). https://doi.org:10.1093/g3journal/jkad220

35 Wijckmans, E. *et al.* Functional and Biochemical Characterization of Alvinella pompejana Cys-Loop Receptor Homologues. *PloS one* **11**, e0151183 (2016). https://doi.org:10.1371/journal.pone.0151183

36 Leclère, L. *et al.* The genome of the jellyfish Clytia hemisphaerica and the evolution of the cnidarian life-cycle. *Nature Ecology & Evolution* **3**, 801-810 (2019). https://doi.org:10.1038/s41559-019-0833-2

37 Durinck, S. *et al.* BioMart and Bioconductor: a powerful link between biological databases and microarray data analysis. *Bioinformatics* **21**, 3439-3440 (2005). https://doi.org:10.1093/bioinformatics/bti525

38 Jaiteh, M., Taly, A. & Hénin, J. Evolution of Pentameric Ligand-Gated Ion Channels: Pro-Loop Receptors. *PloS one* **11**, e0151934 (2016). https://doi.org:10.1371/journal.pone.0151934

39 Krogh, A., Larsson, B., von Heijne, G. & Sonnhammer, E. L. L. Predicting transmembrane protein topology with a hidden markov model: application to

complete genomes11Edited by F. Cohen. *Journal of molecular biology* **305**, 567-580 (2001). https://doi.org:https://doi.org/10.1006/jmbi.2000.4315

40 Katoh, K. & Standley, D. M. MAFFT Multiple Sequence Alignment Software Version 7: Improvements in Performance and Usability. *Molecular biology and evolution* **30**, 772-780 (2013). https://doi.org:10.1093/molbev/mst010

41 Capella-Gutierrez, S., Silla-Martinez, J. M. & Gabaldon, T. trimAl: a tool for automated alignment trimming in large-scale phylogenetic analyses. *Bioinformatics* **25**, 1972-1973 (2009). https://doi.org:10.1093/bioinformatics/btp348

42 Minh, B. Q. *et al.* IQ-TREE 2: New Models and Efficient Methods for Phylogenetic Inference in the Genomic Era. *Molecular biology and evolution* **37**, 1530-1534 (2020). https://doi.org:10.1093/molbev/msaa015

43 Bianchini, G. & Sánchez-Baracaldo, P. TreeViewer: Flexible, modular software to visualise and manipulate phylogenetic trees. *Ecology and Evolution* **14**, e10873 (2024). https://doi.org:https://doi.org/10.1002/ece3.10873

44 Liman, E. R., Tytgat, J. & Hess, P. Subunit stoichiometry of a mammalian K+ channel determined by construction of multimeric cDNAs. *Neuron* **9**, 861-871 (1992). https://doi.org:https://doi.org/10.1016/0896-6273(92)90239-A

45 Hao, Y. *et al.* Integrated analysis of multimodal single-cell data. *Cell* **184**, 3573-3587.e3529 (2021). https://doi.org:10.1016/j.cell.2021.04.048

46 Deryckere, A., Styfhals, R., Elagoz, A. M., Maes, G. E. & Seuntjens, E. Identification of neural progenitor cells and their progeny reveals long distance migration in the developing octopus brain. *eLife* **10**, e69161 (2021). https://doi.org:10.7554/eLife.69161

47 Kuehn, E. *et al.* Segment number threshold determines juvenile onset of germline cluster expansion in Platynereis dumerilii. *Journal of Experimental Zoology Part B: Molecular and Developmental Evolution* **338**, 225-240 (2022). https://doi.org:https://doi.org/10.1002/jez.b.23100

48 Elagoz, A. M. *et al.* Optimization of Whole Mount RNA Multiplexed in situ Hybridization Chain Reaction With Immunohistochemistry, Clearing and Imaging to Visualize Octopus Embryonic Neurogenesis. *Frontiers in Physiology* **13** (2022). https://doi.org:10.3389/fphys.2022.882413

49 Schindelin, J. *et al.* Fiji: an open-source platform for biological-image analysis. *Nature methods* **9**, 676-682 (2012). https://doi.org:10.1038/nmeth.2019

50 Stringer, C. & Pachitariu, M. Cellpose3: one-click image restoration for improved cellular segmentation. *Nature methods* **22**, 592-599 (2025). https://doi.org:10.1038/s41592-025-02595-5

51 Pachitariu, M. *et al.* Suite2p: beyond 10,000 neurons with standard two-photon microscopy. *bioRxiv*, 061507 (2017). https://doi.org:10.1101/061507

52 Bansal, R., Raj, G. & Choudhury, T. in *2016 International Conference System Modeling & Advancement in Research Trends (SMART)*. 63-67.

53 Deryckere, A., Styfhals, R., Elagoz, A. M., Maes, G. E. & Seuntjens, E. Identification of neural progenitor cells and their progeny reveals long distance migration in the developing octopus brain. *Elife* **10** (2021). https://doi.org:10.7554/eLife.69161

Acknowledgements

The authors gratefully acknowledge Denise Walker and all other past and present members of the Schafer and Seuntjens labs for technical assistance and helpful discussions. *Dapnia*

magna were kindly provided by the labs of Robby Stoks and Luc De Meester from KU Leuven, Belgium. The authors thank Joshua Rosenthal from the Marine Biological Laboratory for kindly providing the *Octopus bimaculoides* AChRB1 *Xenopus* plasmid. The authors also wish to acknowledge Gáspár Jékely and Milena Marinković from the Living Systems Institute, University of Exeter, for their advice on the phylogenetic analysis. The authors also wish to thank the Arckens lab for kindly allowing us to use their equipment for the calcium imaging experiments. Jon Howe and the LMB microscopy facilities team offered state of the art imaging facilities and expertise which the authors were very grateful for. The authors are also grateful to Benjamin Jenkins from the University of Cambridge for his expert advice on phylogenetic analysis. We would also like to thank the LMB Scientific Computing team and Rory Bedford for assistance with using the computer clusters. The authors are also grateful to all members of the VisLab team, particularly Elfy Chiang. Finally, the authors wish to thank all support and administrative staff at the LMB and KU Leuven.

Author Contributions

A.C., E.S., and W.R.S conceptualised the project and designed the experiments. A.C. carried out the phylogenetic analysis. E.A. supplied the *O. vulgaris* paralarvae. A.C., I.H., and J.G.R. performed the *Xenopus* oocyte electrophysiology experiments. R.S. and M.Las. prepared *O. vulgaris* and *D. magna* cDNA. A.C., R.S., L.G., M.Lan., and A.M.J. performed the HCR experiments and acquired the images. J.B. developed the HCR image analysis pipeline and A.C. carried out the analysis and visualisation. A.C., R.S., and M.V.D. optimised and carried out the calcium imaging experiments. A.C. and H.A.O. developed the calcium image analysis pipeline and A.C. carried out the analysis and visualisation. A.C., E.S., and W.R.S wrote the original manuscript, and all authors read and critically revised the manuscript. E.S. and W.R.S supervised the project and provided funding/infrastructure.

Funding

This work was kindly supported by the Medical Research Council MC-A023-5PB91 (to W.R.S.), the Research Foundation – Flanders G079521N (to W.R.S.), G040124N (to E.S.) and fellowships 11L1923N (to M.Las) and 1181025N (to M.V.D.), and KU Leuven BOF C14/16/049 (to E.S. and W.R.S.) and ID-N/20/007 (to E.S.).

Declaration of Interests

The authors declare no competing interests.

Materials & Correspondence

Requests for further information and resources should be directed to the corresponding author, William Schafer (wschafer@mrc-lmb.cam.ac.uk).